CENTRO DE INVESTIGACIONES EN ÓPTICA, A.C.

Study of Surface Mechanical Parameters on Composite Biological Structures by using Non-Destructive Optical Tests

Thesis submitted as partial fulfillment for the award of Doctor of Sciences from Centro de Investigaciones en Óptica A.C

Thesis Advisor: Jorge M. Flores Moreno

Thesis co-advisor: Manuel H. De la Torre Ibarra

Presented by:

M.Eng. César G. Tavera Ruiz

October 2019
León, Guanajuato, México

Contents

I. INTRODUCTION 7

1.1 Biological Materials and its Mechanical Structures 7

1.2 Non-destructive optical techniques 11

1.3 Bone structure. An efficient composite material 13

II. THEORICAL FRAMEWORK 15

2.1 Anisotropy and Material Science 15

2.2 DHI fundamentals 16

2.2.1 Holography beginnings 16

2.2.2 Interferometry. A solution for the wavefront reconstruction “problem" 16

2.1.3 Spatial Coherence. 21

2.3 Hologram recording in DHI 24

2.4 DHI system and displacement measurement 26

2.5 Fourier Transform Infrared Spectroscopy 31

III. DHI SET-UP FOR SURFACE STRUCTURAL DAMAGE EVALUATION IN CORTICAL BONE DUE TO MEDICAL DRILLING. 34

3.1 Introduction 34

3.2 Drilled femoral bone preparation 35

3.3 Experimental procedure 37

3.4 Non-drilled bone compression test and results. 41

3.5 Drilled bone compression test and results..... 44

IV. HOLOGRAPHIC INTERFEROMETRIC SYSTEM FOR STUDY OF CORTICAL BONE QUALITY AFFECTATIONS AND THEIR STRENGTH IMPACT. 52

4.1. Introduction..... 52

4.1.1 Bone Affectation classification. 55

4.2 Method..... 57

4.2.1 Bone sample preparation 57

4.2.2 Demineralization process 59

4.2.3 Dehydration method and its collagen affectation 60

4.3. Experimental Procedure..... 60

4.3.1 Fourier transform infrared spectroscopy (FT-IR) validation 60

4.3.2 Compression tests 64

4.3.3 Opto-mechanical system measurement and surface displacements results.. 66

V. SUMMARY AND CONCLUSIONS 71

REFERENCES 75

APPENDIX 86

Illustration Index

Fig.I.1. Bone's hierarchical structure……10

Fig.II.1. Interferometric recording..... 17

Fig. II.2. Linearly polarized plane wave propagation for k vector direction..... 19

Fig. II.3 Coherent scattered light over a rough surface. 23

Fig. II.4. Typical speckle pattern observed on a screen 24

Fig. II.5. Normalized spectral response of a typical monochrome CCD..... 26

Fig II.6 Typical DHI configuration. 27

Fig. II.7 Hologram Intensity distribution map for its linear frequencies fx and fy. 29

Fig. III.1 Schematic of femoral bone samples and the epiphyses structures..... 37

Fig. III.2. Schematic DHI optical system for Surface Structural Damage Evaluation in Cortical Bone..... 38

Fig. III.3. Mechanical press and load cell. 39

Fig. III.4. Compression values to be analyzed and their corresponding load increment Δl=5 lbs during the continuous compression tests. 40

Fig. III.5. Displacement map comparison for three different non-drilled bones.. 43

Fig.III.6. Schematic view as example for a four-cortical drilling (red axes)..... 45

Fig.III.7. Schematic view of pretests different cortical drillings. The observation side is indicated. 45

Fig. III.8. Displacement maps comparison for nine different samples all at 30 lbs. 46

Fig. III.9. Displacement profile for three bones with (a) 2C, (b) 4C, and (c) 6C at 50 lbs. . 47

Fig.III.10. Retrieved displacement maps for three bones with 2C, 4C, and 6C..... 48

Fig.III.11. Retrieved displacement maps for three bones with 2C, 4C for a 6.5 mm diameter drill bit. 50

Fig. III.12. Profile comparison at 200 lbs and 6C drillings with drill bits of 4.5 and 6.5 mm compared to the nondrilled average profile 51

Fig IV.1. Schematic of the cortical bovine bone samples machining steps.. 58

Fig. IV.2. Bone sample groups to be tested. 58

Fig. IV.3. FT-IR mean transmittance spectra comparison for samples with 4 and 6 hours of demineralization (dm + H2O) with respect to the control group (m + H2O). 62

Fig.IV.4. FT-IR mean transmittance spectra comparison for samples with 24 and 48hours of air-drying (m-H2O) with respect to the control group (m + H2O). 64

Fig. IV.5. Mean temporal response for each cortical sample group with region marker for 100 , 200 and 300 lbs 65

Fig IV. 6 DHI set up for the cortical bone compression tests. 67

Fig. IV.7. Average surface displacement map comparison between m + H2O and dm@4hrs + H2O for 100, 200 and 300 lbs. 69

Fig. IV.8. Average surface displacement map comparison between m-H2O@48hrs and dm@4hrs-H2O@48hrs for (a,b) 100, 200 and 300 lbs. 70

Table Index

Table IV.1. Transmittance ratios for the control and demineralization process spectra shown in Fig.IV.3 63

Table IV.2. Transmittance ratios for the control and air-drying process spectra shown in Fig.IV.4 64

Table IV.3. Temporal comparison among sample groups 66

ABSTRACT

In this thesis we report a study on cortical bones by means of the analysis of their surface displacement maps. We use Digital Holographic Interferometry (DHI), a powerful non-destructive optical testing for quantifying micrometric deformations. The bone samples are considered as a biological composite material with anisotropic properties, and as a consequence, with no linear behavior that implies a no repeatable mechanical response, even under the same mechanical excitation signals. This study is divided in two stages; first, cortical bone samples are extracted from porcine femoral diaphysis and cutted into cylinders that match the flat supports of a mechanical press in order to transmit compression loads in the physiological and overload ranges. By using a medical procedure to drill the samples, it was possible to compare the effect of bone loss volume and observe the microfractures presence around the perforations against to those non-drilled samples which were used as reference control. The results show a relationship between bone loss and compression loads that can be assumed as "lower compression values and fewer drillings create higher surface displacements, while higher compression values and more cortical drillings result in smaller surface displacements"; an opposite performance of isotropic materials. This section also proves that the high resolution of DHI gives a better understanding about the bone's microstructural modifications, making it a viable ex-vivo technique to analyze the consequences of some medical procedures. The second section of the study aims to analyze the effect in bone strength when its organic and inorganic components are degraded independently, which simulates bone illness conditions, permitting to unveil their particular role in bone mechanical response. By employing FT-IR spectral signal in transmittance it was possible to validate the effects of demineralization and air-drying procedures implemented on cortical bovine samples that were machinated for compression tests. As in the previous stages, DHI was employed to calculate the amplitude and phase information from the cortical bone samples when are compressed under controlled loads in the physiologic and overload

ranges. The compression tests were managed by a Micro Compressive Testing Machine specially designed for optical non-destructive testing. A comparison in terms of the surface displacement among 1) demineralized, 2) dehydrated, and 3) demineralized and dehydrated groups with those of control, permitted to prove the theory for a strong interrelationship among the hydroxyapatite, collagen and water, which determines the bone strength as well as the role that each one plays.

I. INTRODUCTION

1.1 Biological Materials and their Mechanical Structures

The early parts of the 20th century witnessed the beginnings of the study of biological systems as structures. The first major work on this field is attributed to D'Arcy W. Thompson [1], who looked at biological systems as engineering structures and, from this approach, obtained relationships that described that form. In the 1970's the book "Bone" by Currey [2], exposed a broad variety of mineralized biological materials and their characteristics. "Structural Biological Materials" by Vincent [3] is considered another work of great significance in the area. However, although the field of biology has existed and evolved along this period, the engineering and materials approaches have been often shunned by biologists. Material Science and Engineering represent a discipline that had its inception in the 1950's and has expanded into three directions: metals, polymers and ceramics (with mixtures and composites). Within this scientific route, in the 1990's, Biological Materials have been incorporated to its interests and found its proper future. Many biological systems have shown mechanical properties that are far beyond those that can be achieved using synthetic materials [3,4]. This is an amazing fact when we consider that basic polymers and minerals found in natural systems are weak indeed. The first question within this scientific discipline arises then: ¿What conditions increase strength on this kind of biological systems? Nowadays we know that limited strength in

synthetic materials is a result of the ambient temperature, aqueous environment processing as well as a strong absence of primarily elements such as C, N, Ca, O, Si, and P. In addition, biological organisms are organized in terms of composition and structure, containing both, inorganic and organic components in complex arranges. They are hierarchically organized at nano, micro and meso levels. Material science is being renewed and situated at the confluence of chemistry, physics and biology. From this approach, biological systems are classified in the following areas of research and activity:

- *Biological Materials*: these are the materials and systems encountered in nature.
- *Bioinspired (or biomimicked) Materials*: approaches to synthesizing materials inspired on biological systems.
- *Biomaterials*: these are materials specifically designed for optimum compatibility with biological systems (e.g., implants).
- *Functional Biomaterials and Devices*. Applied devices, conformed by biomaterials, which are devoted for medical and pharmaceutical practice.

Particularly, the study of Biological Materials and systems intends, ultimately:

a) To provide the tools for the development of Bioinspired Materials. This field, also called biomimetics [5], is increasing attention and is one of the new frontiers in materials research.

b) To enhance our understanding of the interaction of synthetic materials and biological structures with the goal of enabling the introduction of new and complex systems in the human body, leading eventually to organ supplementation and substitution. These are the so-called biomaterials.

Hierarchical organization of structure

All materials are hierarchically structured since the changes in dimensional scale bring different mechanisms of deformation and damage. In Biological Materials the hierarchical organization depends on the design while, in synthetic materials, there is often a disciplinary separation based on tradition between materials (material engineers) and structures (mechanical engineers). We can find this hierarchical organization in many complex structures such as bone, abalone shell, crab exoskeleton, to mention a few.

In bone for example, the building block of the organic component is the collagen, which is a triple helix with diameter of approximately 1.5 nm. Collagen is a rather stiff and hard protein. It is a basic structural material for soft and hard bodies, it is the main load carrying component of blood vessels, tendons, bone, muscle, etc. In bone, these molecules are intercalated with the mineral phase (hydroxyapatite, a calcium phosphate) forming fibrils that, on their turn, curl into helicoids of alternating directions. These, the osteons, are the basic building blocks of bones. The hydroxyapatite crystals are platelets with a diameter of approximately 70–100 nm and thickness of ~ 1 nm. The volume fraction distribution between organic and mineral phase is about 60/40, making bone unquestionably a complex hierarchically structured biological composite [6].

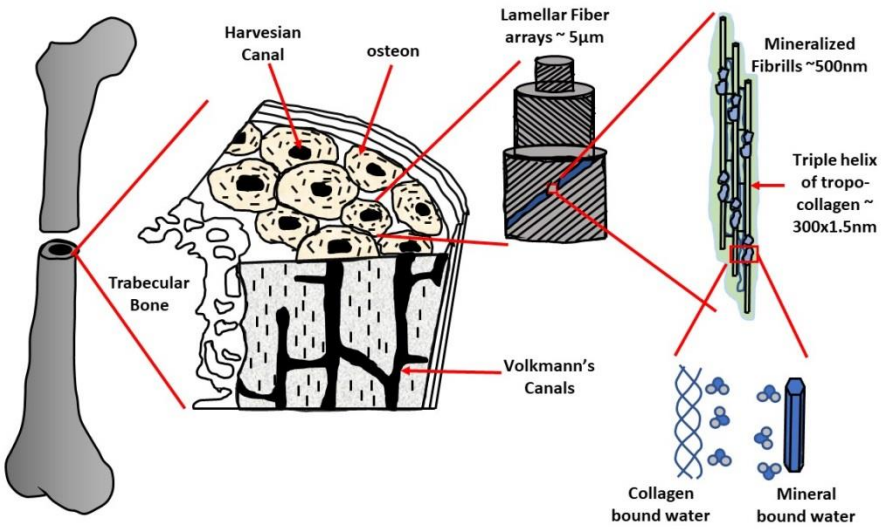

Fig.I.1. Bone's hierarchical structure

Multifunctionality and self-healing

Most biological materials are multifunctional [4]; they accumulate functions such as:

- *Bone*: structural support for body plus blood cell formation.
- *Chitin-based exoskeleton in arthropods*: attachment for muscles, environmental protection, water barrier.
- *Sea spicules*: light transmission plus structural.
- *Tree trunks and roots*: structural support and anchoring plus nutrient transport.
- *Mammalian skin*: temperature regulation plus environmental protection.
- *Insect antennas*: they are mechanically strong and can self-repair. They detect chemical and thermal information from the environment and can change their shape and orientation.

Another main difference of biological systems, in contrast with current synthetic systems, is their self-healing ability. Most structures can repair themselves, after undergoing trauma or injury. Exceptions like teeth and cartilage do not possess any significant vascularity, limiting its nature to

exchange damaged tissue and get nutrients. It is also true that brains cannot self-repair; however, other parts of the brain can take up the lost functions [6].

A good Biological Material representative

As it can be seen, Biological Materials are complex to be analyzed from only one approach and the extent and complexity of the subject will require time enough of global research effort to be elucidated. In this thesis we study surface mechanical behavior of cortical bone due to it well represents a complex Biological Material where structures with different dimensions at organic and inorganic phases, make it worth of study under different conditions. Works concerning the mechanical properties of bone have been carried out in several areas, such as clinical [7], engineering (material science) [8], physics [9] and mathematical models [10]. We use a noninvasive technique which expresses qualitative and quantitative information. The resulting data aim at getting a better understanding about the microstructural variations of the bone and how its composition and structure rule its behavior.

1.2 Non-destructive optical techniques

From a technical point of view, the non-destructive testing (NDT) techniques are defined as analytical procedures used in science and industry to evaluate the properties for a material, component or system without causing damage to them [11]. Particularly, *optical* NDT technologies present higher detection accuracy and sensitivity, accessible signal processing, non-invasiveness, and resistance to electromagnetic interference [12]. In the field of interferometric techniques, the integration of new sensors and lasers creates a new group of optical NDT systems based on *speckle*. Speckle is the minimum spatial unit of interference that a coherent light source can produce on a particular vision element, due to the scattering of light over or through the sample. The possibility to

track or correlate speckle in time or space makes it possible to measure changes in the surface sample in the range of microns with a very high sensitivity [13]. In order to retrieve the speckle information coming from the sample, several methods were adapted to basic interferometry; however, NDT techniques which appeared with speckle produced by lasers, are considered as fundamental as they are employed to solve a variety of problems in structural mechanics for industry and science [14]. These methods are Laser Speckle Correlation (LSC), Electronic Speckle Pattern Interferometry (ESPI), and Digital Holographic Interferometry (DHI), which are widely applied in the characterization of several materials under specific conditions to perform structure displacements associated to its external and internal deformations [15-17]. The effectiveness of these techniques is not only limited to homogeneous, but also, to so-called *composite materials*, where two or more single materials are combined in different structural geometries and with different proportions to generate a different mechanical property that otherwise could not be achieve separately [18-20]. Some composite materials present non-linear and non-isotropic mechanical responses; thus, maintaining same experimental conditions for testing, do not guarantee total repeatability in their structural deformations. Many alternative techniques have tried to deal with the issue of predictable models for mechanical response on composite materials; such as Finite Element Models (FEM) or the Virtual Fields Method (VFM) [21]. In FEM and VFM, the primary goal consists on modeling iteratively a set of force functions based on experimental results. These functions act within the material geometry and the one that is closer to the real deformations solves the model. The main limitation of these alternative methods lies in the so-called “boundary conditions”. For a real model, it is necessary to know the traction forces along the sample. This fact is only measured in practice, so, the final results perform an approximation that not necessary will predict non-linarites on composite materials [21-23]. This non-linear and anisotropic nature increases and becomes hard to be characterized by using alternative techniques like FEM and VFM for biologic composite materials. The high sensitivity of samples (in-vivo or ex-vivo) reacts rapidly to external stimulus and

consequently the parameters that regulate their mechanical properties could change in real time [24]. It is on this field where optical NDT techniques are especially reliable for measuring mechanical properties in samples that behave in this manner. The non-contact and non-invasive nature of NDT techniques help to evaluate mechanical properties in composite biomaterials with any alteration provoked by them. Specially, from the NDT based on speckle techniques, DHI performance does not require any movable element within its interferometric hardware; only two images are needed to calculate the full-field displacement information; thus, real time DHI systems are ideal in fast mechanical evaluation, particularly when the behavior of the sample is not repeatable [25-27].

1.3 Bone structure. An efficient composite material

As it is mentioned before, the bone is a composite material formed by three primary constituent elements: (1) fibrillary type 1 collagen (35 to 45% of the volume), (2) mineral linking of calcium phosphate in the form of semi-crystalline hydroxyapatite (35 to 45% of the volume), and (3) water (15 to 25% of the volume). This complex biphasic constitution (organic and inorganic structures) results into an extremely efficient biomaterial if lightness and resistance of it are compared to other materials; so, structurally, the bone is understood as an *intelligent material* that gives support to the human body at the time that protects its vital organs [28-29]. But the role of bone in humans goes far beyond. From its metabolic functionalization, the bone performs as a reservoir of main minerals, such as phosphor and calcium that depending on the demand, are delivered gradually through the blood system. The Long bone red marrow is responsible of blood cell formation and the yellow marrow acts directly on the homeostasis process. Finally, the bone is considered as an endocrine organ since its production of osteocytes and osteoblasts helps the kidney and pancreas to regulate the abortion and secretion process of several substances such as osteoclastine and insulin among others [30-31]. All these properties make the bone an interesting material, work of study for many research groups in different areas of science since biologic and medical, to engineering and

physics. Along this work, a wide study on cortical bone structures is presented based on surface displacement analysis under different conditions. In all cases, bone tissues were observed by means of a DHI system designed specifically for the mechanical tests. The corresponding results are included in chapter III and IV.

In the first stage of the thesis we focus on the traumatological treatment of bone's fracture process and the structural dynamics that medical healing procedures involve. Bone fractures could be produced by an excessive, repetitive, or sudden load. A regular medical practice to heal it is to fix it in two possible ways: external immobilization, using a ferule, or an internal fixation, using a prosthetic device commonly attached to the bone by means of surgical screws. In the corresponding experimental work of this section, cortical porcine bones were treated for medical drilling procedure in order to compare them to their corresponding healthy group when compressive load was applied. The results are presented as pseudo 3D mesh displacement maps for comparisons in the physiological as well as overcharge range of load. A particular relationship between compression load and bone volume loss due to the drilling is analyzed.

In the second stage of the work, we studied the anisotropic nature of the bone structure and how it is related to the bone strength and its composition. Bone strength is a complex property determined mainly by three factors: quantity, quality and turnover of the bone itself [32]. Most of the patients who experience fractures due to fragility could never develop affectations related to bone mass density (i.e. osteoporosis). The effect of secondary bone strength affectations is analyzed by simulating the degradation of one or more principal components (organic and inorganic) while they are inspected with DHI. A strong correlation among the hydroxyapatite, collagen and water is found and mechanically is evidenced that mineral density is not only the main determinant in bone strength as it is now clinically accepted.

II. THEORICAL FRAMEWORK

2.1 Anisotropy and Material Science

Derived from Greek isos “equal” and tropos “way”, isotropy property means uniformity in all directions, and precise definitions will always depend on the subject area; for example, in radiometry, isotropic radiations concerns phenomena that involves the same intensity of light regardless of the direction of measurement; particularly at Material Science in the study of mechanical properties, isotropic means having identical property for all directions. Metals and glass are examples of isotropic materials. Isotropic materials are easy to shape, and its behavior are easier to predict. On the other hand, anisotropic materials can be adaptable to the forces that an object is expected to experience, and they do not behave equally for the different directions, so they are harder to predict. Examples of artificial anisotropic materials are laminated steel, whose anisotropy is induced by the lamination process, and composite materials, where the union of an isotropic matrix and aligned fibers or tissues gives a final material that is macroscopically anisotropic. At a larger scale, some structures can be modeled as anisotropic shells or membranes. Also structures and materials created by Nature can be anisotropic, like pack ice, leaves, wood and bones, where the matter is organized along preferential directions (e.g. along the vertical one) for biological reasons [33]. Particularly, the complexity of cortical bone also arises from its hierarchical structural organization as it was mentioned before. The anisotropy may be partly due to the highly anisotropic structure of mineralized collagen fibrils (see section 1.1). The fibrils are found as bundles or aligned arrays, and these can be arranged in a variety of different patterns, resulting in different mechanical properties in all three orthogonal directions. Although the patterns of lamellae are still a matter of discussion, many researchers have indicated that cortical bone has orthotropic material properties [34].

2.2 DHI fundamentals

2.2.1 Holography beginnings

At the ends of the forties, in the nineteenth century, the optical "wavefront reconstruction" method was discovered by the Hungarian Physicist Dennis Gabor (1900-1979, UK). Gabor showed a novel two-step, lensless imaging process which we now know as holography. He proved that when a coherent reference wave is simultaneously overlapped with the light diffracted by or scattered from an object it is possible to record the relative information of both waves such as the amplitude and the phase no matters that the recording media responds only to the light intensity. This means that from an interference pattern recorded on a 2D element, a 3D-image of the original object can be obtained. This is why Gabor named this wavefront reconstruction method as *Holography*, which origins from the greek word-composition *Holos*-total, and *Gramma*-register; that is to say, "*record of a whole*". In the beginnings this imagine technique had poor interest, but with technological developments such as the Laser and more sensitive sensors, the 1960s witnessed deep improvements that extended its applicability. Finally, Dennis Gabor received the Nobel prize in physics (1971) for his discovery.

2.2.2 Interferometry. A solution for the wavefront reconstruction "problem"

The primary goal in holography consists on recording and reconstructing both, the amplitude and the phase of an optical wave coming from a coherently illuminated object. In principle, all recording media are only sensitive to light intensity, thus, it is necessary to find *a way to convert phase information to intensity variations* for recording purposes. The solution for this problem is given by the interferometry phenomena; that is, a second wavefront mutually coherent with the first and of known amplitude and phase, is added to the unknown wavefront. The intensity of the sum of two complex fields then depends on both, the amplitude and phase of the unknown field.

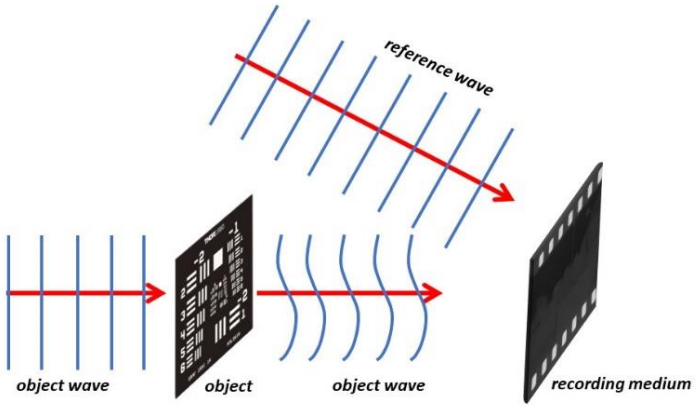

Fig.II.1. Interferometric recording (transmittance configuration)

A practical model for electromagnetic waves description can be stated by means of the temporal and spatial dependence of its electric intensity vector $\vec{E}$. The simplest form corresponds to a plane wave linearly polarized. If a wave of this type propagates in z direction, its three components of $\vec{E}$ can be written as:

$$E_x = 0$$

$$E_y = A\cos(wt - kz) \tag{II.1}$$

$$E_z = 0$$

where A corresponds to the amplitude of the wave, w to its angular frequency, and k to its wave number; and they are primary defined as:

$$w = 2\pi\nu \tag{II.2}$$

$$k = \frac{2\pi}{\lambda} \tag{II.3}$$

And, for these expressions, ν is known as temporal frequency and λ as the wavelength of light. Visible light frequency oscillates in the order of $10^{15}[Hz]$ and λ ranks from 0.38 to 0.76 μm. Light wave also possess a phase velocity described by $v = \frac{w}{k}$, which depends on the propagation medium. The maximum value for this quantity occurs in the vacuum and its constant value is $c = 3 \times 10^8\ [m/s]$. The wave expressed in Eq. (II.1) is classified as plane wave because in any temporal and spatial point, E_y presents the same value for all the points placed in a normal plane to the propagation direction. This wave is also named as linearly polarized due to its constant oscillation along *y* axis. In a general view, $\vec{k}$ vector points the propagation direction of the electromagnetic wave and its magnitude k corresponds to $\frac{2\pi}{\lambda}$; as consequence, in a plane wave, E presents the same intensity value for all the points in a normal plane to $\vec{k}$ [35].

Let's consider $\vec{r} = x\hat{\imath} + y\hat{\jmath} + z\hat{k}$ as the position vector of any point into a plane that an observer is looking at. Considering the general form of wave propagation in Eq. II.1 and from Fig. II.2 where the plane wave linearly polarized travels in $\vec{k}$ direction, the electric intensity vector for the observer can be described as:

$$E_{x'} = 0$$

$$E_{y'} = A\cos\left(wt - \vec{k}.\vec{r}\right) \tag{II.4}$$

$$E_{z'} = 0$$

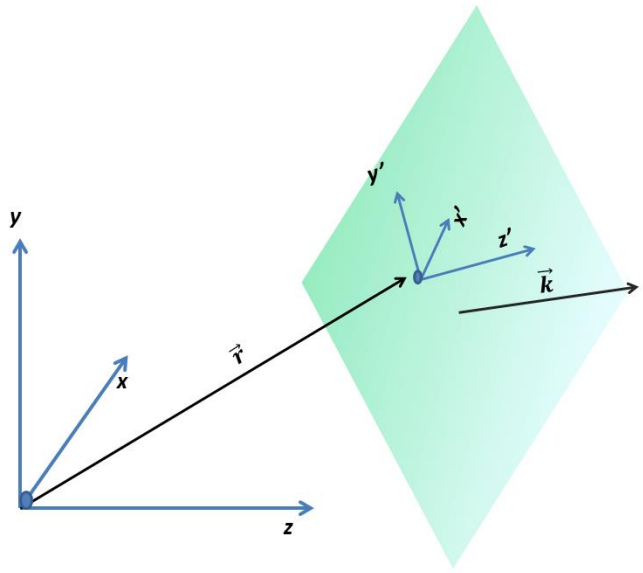

Fig. II.2. Linearly polarized plane wave propagation for k vector direction

Optical detectors are not able to respond to 10^{15} [Hz], the frequency value of electromagnetic field oscillation of light. Instead of that, they detect the temporal mean of the light intensity oscillations through its surface; then they are sensitive to irradiance I.

This quantity can be defined in terms of its electric intensity vector such as:

$$I = \varepsilon v \langle E^2 \rangle \tag{II.5}$$

where ε is the electric permittivity of the medium where light is traveling in, and v is the propagation velocity. So, as it can be seen, I behaves proportional to the temporal mean of E^2, and then, for computing, the εv constant is commonly omitted.

Once these quantities have been described, it is necessary to begin with an interference analysis. Let's suppose two different waves that superpose each other with electrical vector intensities E_1 and E_2 which oscillate at the same frequency and both are linearly polarized. Given that $E = E_1 + E_2$, then:

$$I = \langle E^2 \rangle = \langle E_1^2 \rangle + \langle E_2^2 \rangle + 2\langle E_1 . E_2 \rangle \quad \text{(II.6)}$$

and for the scalar development:

$$E_1 = A_1 \cos(wt - k_1 . r) \quad \text{(II.7)}$$

$$E_2 = A_2 \cos(wt - k_2 . r + \emptyset) \quad \text{(II.8)}$$

where $\emptyset$ corresponds to a constant relative phase between both waves. Combining equations II.6 to II.8 and applying the mean value, the interference intensity is commonly written as:

$$I = I_1 + I_2 + 2\sqrt{I_1 I_2} cos\delta \quad \text{(II.9)}$$

where:

$$I_1 = A_1^2 \quad \text{(II.10)}$$

$$I_2 = A_2^2 \quad \text{(II.11)}$$

and:

$$\delta = k_2.r\text{-}k_1.r - \emptyset \qquad \text{(II.12)}$$

Thus, in any place of the path that both waves travel, the spatial length between them is a constant magnitude determined by δ. Equation (II.9) is frequently identified as the general model of interference, which shows that the irradiance of the interference varies around a background value $(I_1 + I_2)$ and the interference phenomena is in fact modulated by a cosine function that delivers a minimum intensity value $I = I_1 + I_2 - 2\sqrt{I_1 I_2}$ at all the points where $\delta = (2n+1)\pi$, and a maximum intensity value $I = I_1 + I_2 + 2\sqrt{I_1 I_2}$ at all the points where $\delta = (2n)\pi$, provided n is in the integer domain. Finally, the outcoming fringe pattern helps to measure the spatial distribution of the optical phase difference between both waves; and as it was explained, it can be recorded by exposing a photographic film to the light scattered by a diffuse plane, or such as it occurs at the current work, by recording in a digital sensor. [35]

2.1.3 Spatial Coherence.

At this point of the manuscript, it has been defined the interference phenomena which relates interference irradiance patterns that helps to reconstructing both, the amplitude and the phase of an optical wave coming from a coherently illuminated object. Now is then necessary to explain what "coherently illuminated object" means.

In chapter I it was stated that "speckle is the minimum spatial unit of interference that a coherent light source can produce on a particular vision element, due to scattering of coherent light spread over or through a sample". Numerically, when an object is illuminated by a light source, each object point on the surface represents an element that generates an amplitude impulse response in the image plane. If the phase amplitudes of the light at a particular object point vary randomly with time,

then the overall phase amplitudes of the impulse response will vary in a corresponding manner. Then, the statistical relationships between the phase amplitudes at those points on the object will influence the statistical relationships between the corresponding impulse responses in the image plane. These statistical relationships will greatly affect the result of the time-averaging operation that yields the final image intensity distribution. That's why, in terms of interferometry, we classify light in two groups depending on illumination type. In the first group, we consider object illumination with the particular property that the phase amplitudes of the field at all object points vary coordinately respect to time. Although any two object points may have different relative phases, their absolute phases are varying respect to time in a perfectly correlated form. Such illumination is called ***spatially coherent*** and it is the type of light that interferometry uses. In the second group, we consider object illumination with the property that phase amplitudes at all points on the object are varying in totally uncorrelated manner. Such illumination is called ***spatially incoherent***. Coherent illumination is obtained whenever light appears to originate from a single point and due to its coordinated emission. The most common example of a source of such light is a laser, although more conventional sources (eg. zirconium arc lamps) can yield coherent light (of weaker brightness than a laser), if their output is first passed through a pinhole. Incoherent light is obtained from diffuse or extended sources, for example gas discharges and the sun [35-36].

Speckle phenomena occurs whenever coherent light fall on a rough optical surface, which means that the amplitude of surface irregularities is in the order of the wavelength (λ) of the incident light, inducing a light scatter in all directions as can be seen at figure II.3; [24], [37].

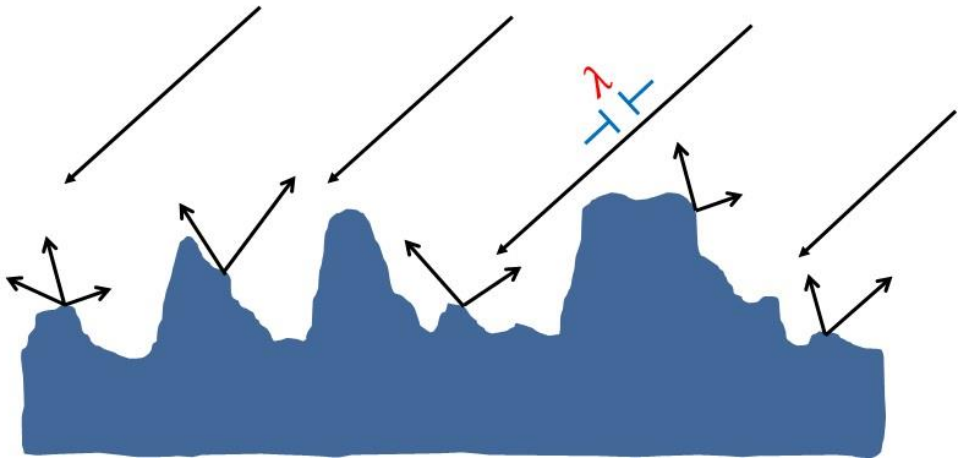

Fig. II.3 Coherent scattered light over a rough surface.

Scattered light provokes mutual interference of many wavefronts individually dispersed, giving rise to interference patterns that are conformed by dark and brilliant points named speckle. These shiny spots are distributed randomly along the tridimensional space where the wave fronts cross each other. Figure II.4 shows a typical speckle pattern.

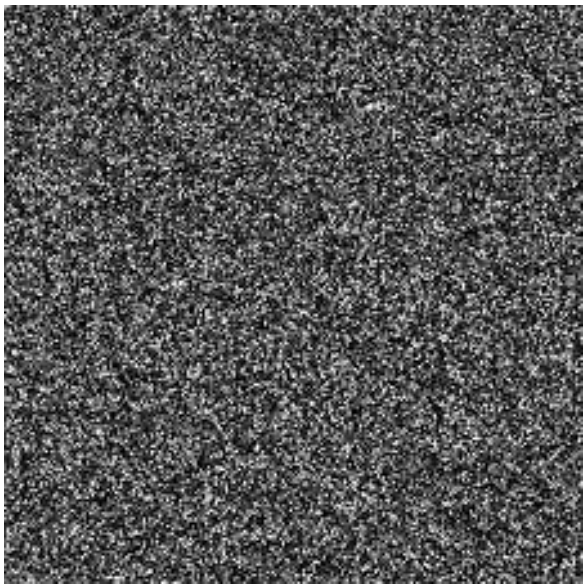

Fig. II.4. Typical speckle pattern observed on a screen

2.3 Hologram recording in DHI

Nowadays, hologram recording is made by using digital vision sensors, typically, based on Coupled Charge Devices (CCD) or Complementary Metal-Oxide-Semiconductor (CMOS) technologies. Digital image information is stored for quantitative analysis by mean of computer systems. The method for quantitative phase determination that holography commonly uses is the Fourier Transform evaluation, which maps the irradiance energy in terms of frequency obtained from interference patterns.

A digital camera is an electronic device that captures images information in terms of electric charge and is configured to record a scanning line or a surface area from transmitted or reflected light in contact with an object. Any camera that is selected for hologram recording must be able to solve the resulting interference pattern when the reference and object wave are combined over the sensor area [38]. The maximum spatial frequency f_{max} for correct hologram recording is determined by a maximum angle θ_{max} between both wave fronts according to the next equation:

$$f_{max} = \frac{2}{\lambda} \sin \frac{\theta_{max}}{2} \tag{II.13}$$

In practice, this frequency is also calculated in terms of the distance between two consecutive pixels Δx on the sensor:

$$f_{max} = \frac{1}{2\Delta x} \tag{II.14}$$

Equation (II.14) clearly expresses that the maximum interference frequency in the interference pattern requires two digital sampling units (pixels) to be solved, which is the equivalent to Nyquist theorem for electronic comunication theory. By combining equations (II.13) and (II.14), θ_{max} is expressed as:

$$\theta_{max} = 2 \sin^{-1}\left(\frac{\lambda}{4\Delta x}\right) \approx \frac{\lambda}{2\Delta x} \tag{II.15}$$

where the aproximation is accepted to small angles (in practice, less than 10 degrees) [37]. The spectral range for camera sensors is selected to satisfy the experimental requirements, but a general purpose based-silice devices typically offers a monochromatic functional range between 400 and 1000 nm with a common dynamic range of 8 bits (256 intensity levels) which is far away from originary photographic film resolution, but enough for hologram intensities recording. See figure II.7.

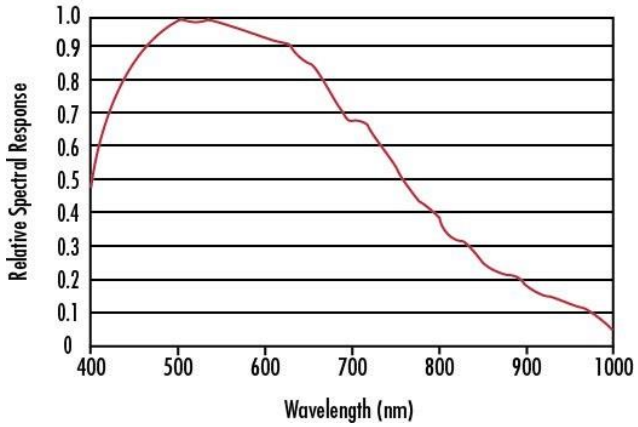

Fig. II.5. Normalized spectral response of a typical monochrome CCD. Image taken from www.edmundoptics.com

2.4 DHI system and displacement measurement

Figure II.6 shows a typical configuration used in DHI, where a laser beam is divided in the object and reference beam by means of a beam splitter BS and then passed through the spatial filters SF1 and SF2. The object under study is then illuminated by the object beam and the dispersed light coming from the object is collected by mean of a lens L with an aperture A in front of it. By using a beam combiner BC, the reference and the object light are superposed over the CCD camera sensor. The interferogram images that result by this process are digitalized and recorded by the camera and then, saved in a local memory for subsequent processing. A worth mention fact is that during the interferogram acquisition process it is necessary to provide the system with stable mechanics, in that, any external vibration can cause considerable differences between object and reference optical path length. These differences give rise to possible decorrelated phase interferograms that limit any object displacement analysis. With the aim to avoid this “mechanical noise” it is recommended to place the optical setup over an isolated optics table which minimizes the vibration effect.

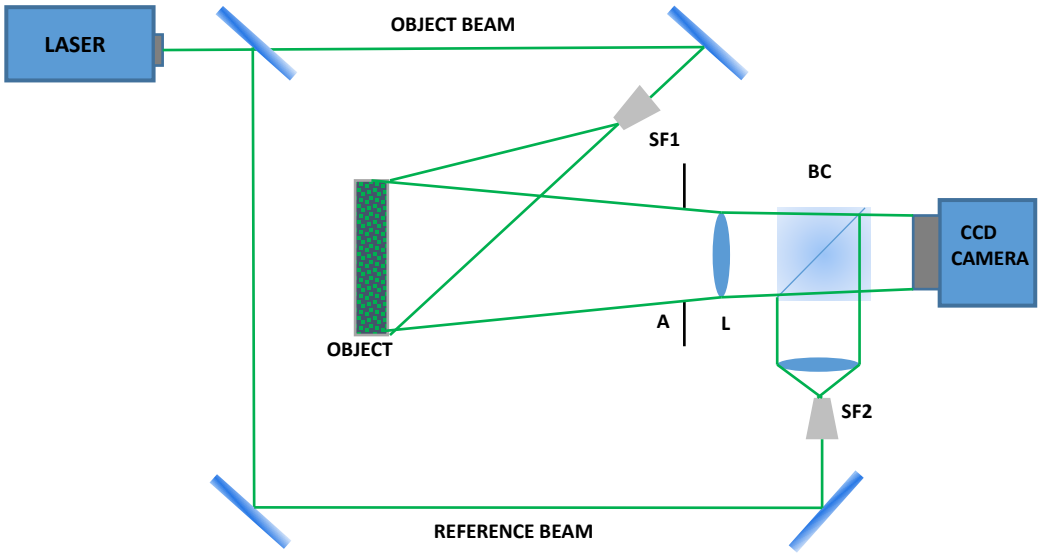

Fig II.6 Typical DHI configuration.

DHI technique uses the double exposure method for obtaining fringe patterns related to quantitative displacements over the surface of the deformed object. The method uses two consecutive images (holograms) of the object which correspond to different sample states; one image is acquired before and the second image after that a deformation is applied. As each hologram consist of the superposition of the reference and object beams over the sensor [39], the total pattern interference intensity is expressed as:

$$I(x,y) = |R(x,y) + O(x,y)|^2 \tag{II.16}$$

where R and O express the complex amplitude wavefronts for reference and object beams respectively. Their instantaneous punctual amplitude depends on the location over its rectangular-coordinate plane XY as follows.

$$O(x,y) = o(x,y)\exp\left[i\varphi(x,y)\right] \quad \text{(II.17)}$$

$$R(x,y) = r(x,y)\exp\left[-2\pi i(f_x x + f_y y)\right] \quad \text{(II.18)}$$

From equations II.17 and II.18, while $\varphi(x,y)$is the optical phase for the light dispersed from the object surface, $2\pi f_x x$ and $2\pi f_y y$ represent the optical phase for the respective directions x and y expressed in terms of their linear spatial frequency f for the reference wavefront. By substituting II.17 and II.18 equations in II.16, it is possible to express:

$$I(x,y) = a(x,y) + c(x,y)exp\left[2\pi i\left(f_x x + f_y y\right)\right] + c^*(x,y)exp\left[-2\pi i\left(f_x x + f_y y\right)\right] \quad \text{(II.19)}$$

which represents the hologram intensity where the energy distribution for the interference phenomena has scattered for real *c* and conjugated complex *c** interference orders [40].

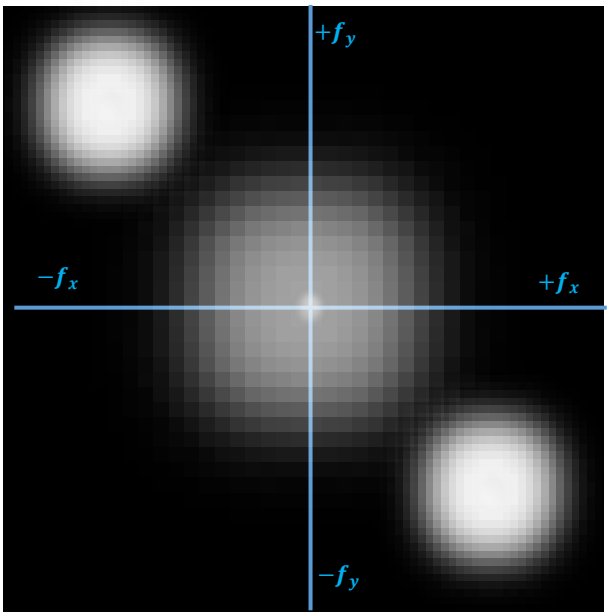

Fig. II.7 Hologram Intensity distribution map for its linear frequencies fx and fy. The simulation shows the real c term in the (-fx ,+fy) quadrant, the conjugated complex c term in the (fx ,-fy) quadrant, and the zero order of interference in Eq. II.19 at the center.*

The complex amplitude wavefront $a(x,y)$ conforms the backlight in the hologram intensity and, $c(x,y)$ and $c^*(x,y)$, the modulation of this intensity pattern; all of them, expressed in terms of the object and reference beams amplitudes $o(x,y)$ and $r(x,y)$, respectively, as it is shown by equations II.20 and II.21.

$$a(x,y) = o^2(x,y) + r^2(x,y) \tag{II.20}$$

$$c(x,y) = o(x,y)r(x,y)exp[i\varphi(x,y)] \tag{II.21}$$

In order to determine the change in the optical phase information due to deformations in the object, a Fourier Transform algorithm processing is applied to the hologram intensity, corresponding to the reference state of the object in the form of Eq. II.19; [41]. Once this interference pattern is

expressed in spatial frequency domain, it is filtered from the DC term $a(x, y)$ and from the complex conjugated $c^*(x, y)$ wavefront. This is possible since $c(x, y)$ and $c^*(x, y)$ contain the same absolute spectral information. The remaining term $c(x, y)$ is then calculated for the spatial domain applying the Inverse Fast-Fourier Transform algorithm (IFFT). At this point, its spatial distribution can be expressed as follows:

$$\varphi(x, y) = arctan \frac{Im[c(x,y)]}{Re[c(x,y)]} \tag{II.22}$$

Afterwards, once the stimulus has been applied to the sample, the whole process is repeated for the intensity pattern associated to the deformed state in the object, and then, it is possible to obtain the corresponding optical phase $\varphi'(x, y)$.

The relative optical phase concerning to the external deformation is then calculated by subtraction of the reference optical phase $\varphi(x, y)$ from the deformed optical phase $\varphi'(x, y)$. Hence, for any corresponding pair reference-deformation of the optical phase distribution, it is possible to express:

$$\Delta\varphi(x, y) = \varphi' - \varphi \tag{II.23}$$

The relative phase difference $\Delta\varphi(x, y)$ is obtained as a *wrapped phase* map, which contains the deformation information codified within a range of $-\pi$ to π values, (black and white, respectively) as it solves a tangent function in II.22. This phase map is unwrapped using a numerical algorithm that stitches the discontinuity jumps from $-\pi$ to π to obtain a smooth optical phase map,

which is then converted into a displacement map d when it is related to the sensitivity vector s defined by the geometry of the interferometric array as II.24 shows [42]:

$$\varphi(x,y) = \frac{2\pi}{\lambda}\left(\bar{d}\cdot\bar{s}\right) \tag{II.24}$$

In the particular case of the out of plane deformation sensitivity, II.24 reduces to:

$$\varphi(x,y) = \frac{2\pi}{\lambda}(1+\cos\theta)w \tag{II.25}$$

where λ is the laser's illumination wavelength, θ is the angle between the illumination and the observation directions, and w is the perpendicular to the object's surface displacement component. The latter is valid when small angles θ are used (normally less than 10°) [37], [41], [43].

2.5 Fourier Transform Infrared Spectroscopy

Fourier transform infrared spectroscopy (FT-IR) is a technique which is used to obtain an infrared spectrum of absorption, emission, photoconductivity or Raman-scattering of solid, liquid or gas. This technique collects data in a wide spectral range. Specifically, Infrared (IR) radiation wavelength is divided into:

- Near (NIR: 10,000 – 4,000 cm-1)
- Middle (MIR: 4,000 – 200 cm-1)
- Far (FIR: 200 – 10 cm-1)

Its potential relies in that each of different material is a unique combination of atoms, then no two compounds produce the exact IR spectrum. This fact results in a positive identification

(qualitative analysis) for every different kind of material. In addition, the intensity of the signal detection in the spectrum represents a direct indication of the amount of material present, fact that combined with modern algorithms have boosted IR spectroscopy as an excellent tool for quantitative analysis.

There are three basic spectrometer components in an FTIR system: radiation source, interferometer and detector.

All the manufacturers use a heated ceramic source which is more often water-cooled. The composition of the ceramic and the method of heating vary but the aim is the same, the production of a heat emitter that is able to operate at high temperatures as possible while the life of the instrument is preserved. Heated objects emit at all FT-IR wavelengths and this emission increases with temperature.

The interferometer divides radiant beams, generates an optical path difference between them, and after one of the beams passes through the sample, recombines them in order to produce repetitive interference signals measured as a function of optical path difference by the detector (controlled spectrum). As its name implies, this interferometer produces interference signals, which contain infrared spectral information of the sample. This is what helps us to identify unknown materials; determine the quality or consistency of a sample and it is also possible to determine the number of components in a mixture.

Most detectors in FT-IR systems act as photo resistors due to the fact that they have a very high resistance in the dark and this falls as light falls on them. The most sensitive are the Ge and InGaAs semi-conductor devices. In the dark, they can have resistance magnitudes as high as $3x10^8$. Measuring resistance at these high values and doing so rapidly requires the use high quality electronics if spurious signal (noise) is not permitted on detected signal. All semi-conductor detectors show absorption bands, then they will ignore radiation longer than a characteristic wavelength. Cooling detectors invariably reduce the amount of noise they develop.

Some of the major advantages of FT-IR over the dispersive techniques (i.e. grating monochromator technique) include:

Speed: In that all the frequencies are measured simultaneously, most measurements by FT-IR are made in a matter of seconds rather than several minutes. This is also known as the Felgett advantage.

Sensitivity: Sensitivity is strongly improved with FT-IR for many reasons. The detectors employed are very sensitive, the optical throughput is much higher which results in much lower noise levels, and the fast scans make possible to include several scan loops to reduce the random measurement noise to any desired level.

***Mechanical Simplicity*:** A unique mirror in the interferometer is the only continuously Moving part in the instrument; then, there is very little possibility of mechanical breakdown.

Internally Calibrated: These instruments employ a He-Ne laser as an internal wavelength calibration standard. These advantages, along with several others, make measurements made by FT-IR extremely accurate and reproducible. Thus, it is a very reliable technique for positive identification of virtually any sample [44].

III. DHI SET-UP FOR SURFACE STRUCTURAL DAMAGE EVALUATION IN CORTICAL BONE DUE TO MEDICAL DRILLING.

3.1 Introduction

A bone is fractured if its continuity is broken, but it can heal itself producing new bone cells and blood vessels in and around the fracture. Basically, two approaches treat a fracture: the conventional and the direct form. In conventional treatment the immobilization process is from the outside. This is a viable option in minor injuries where no surgery is required, but in a major trauma the limitation of this technique is the complication to optimally align, from the outside, all the bone parts that results in long healing times. This alignment issue is not present in the direct approach where the bone's fixation is made internally using immobilization screws, wires, and plates. This technique implies removal of the bone's material by drilling to fix the prosthetic device with screws [45]. When the drilling process is performed, the bone's temperature should not rise beyond a safety threshold to avoid a localized necrosis (irreversible death of the bone's cells) [46]. When this threshold is overcome, and a necrosis is generated, the result it's a poor screw fixation. The latter results in a slow bone healing time because physiological forces acting on the fixation demand a high stability of the prosthetic device and then the new bone formation cannot be reinforced adequately [47]. In addition, the bone drilling presents structural resistance and large vibrations, making it difficult to grip the hand piece, or in extreme cases, breaking the drill bit [48-49]. To ensure the fixation of the screw's threads, the person performing the procedure must grip the bone to enclose the drilled hole, but possible necrosis causes breakdown of the bone (crystalized dead tissue) around the implantation site leading to the loosening or misalignment of the fixation [45]. In some cases, it

is necessary to use a wider drill bit to compensate the lack of grip with the loss of bone material that this involves.

3.2 Drilled femoral bone preparation

To analyze how the cortical drilling process affects the surface's structural response of a large bone, a study in porcine femoral bones with and without the presence of cortical drillings is performed. An out of plane sensitive digital holographic interferometer is used to retrieve the optical phase during a controlled compression test. This configuration is selected because it shows sensitivity in the perpendicular to the bone's surface axis (z), where the immobilization screws may show the largest movement/release. The test simulates physiological and overload compressions in the range of 30 to 400 lbs. All the analyzed bones were taken from the porcine strain *Landrace*. They are less than 24 hours post-mortem samples from healthy non-drilled femurs from the back leg of male animals (for human consumption) with a weight rank between 195 and 205 lbs and five months old. The separated femora were submerged in soft chlorine water solution (1%) for about 120 min. This was useful to clean out the muscles and connective tissues using a scalpel to get a whiter bone surface and avoid damage on it (such as in the case of concentrated acid solutions). All tests were carried out at room temperature within a period of 15 min. Surface structural response comparisons among several bones with a different number of cortical drillings are presented as full-field high-resolution displacement maps retrieved from the optical phase.

For this study it is important to remember, as it was mentioned in the previous sections, that digital holographic interferometry is not only a noninvasive and a noncontact technique with a high sensitivity and resolution; but it is also a technique that does not need any moving elements within the interferometer's arrangement to retrieve the optical phase. The resulting qualitative and quantitative information gathered with this system, such as displacement behavior and magnitude for

physiologic and overload compressions, will complement those studies on bones that use techniques such as micro-indentation, CT scan, and ultrasound [50-53]. The resulting data aim at getting a better understanding about the microstructural variations of the bone when it is subjected to this procedure.

For this case of study where the surface response is investigated in a large bone, an acceptable model for a human bone could be found in a porcine one. This comparison is based in previous studies where chemical and structural characterizations are reported [54-55]. The bone has a viscoelastic behavior that responds differently according to the speed and magnitude of the applied load. This tissue supports high loads when they are applied in a short time; however, if these loads are applied slowly, the bone breaks in low-load magnitudes [55]. The sample selected for this analysis is a femoral bone in which the response of the diaphysis is of particular interest (refer to Fig. III.1). The structural response on the diaphysis's surface comprises all the internal movements of the cortical bone as well as the absorbing influence of the cancellous bone. To avoid this non-controllable absorption response (nonlinear factor), the bone is sectioned to test only the diaphysis by cutting the proximal and the distal epiphyses (red-dotted line in Fig. III.1). Furthermore, the femoral diaphysis is large enough to drill holes with a separation of 12 mm between them (a common length used in medical procedures) and is a regular surface, allowing it to be positioned at exactly the same reference location during the different compression tests.

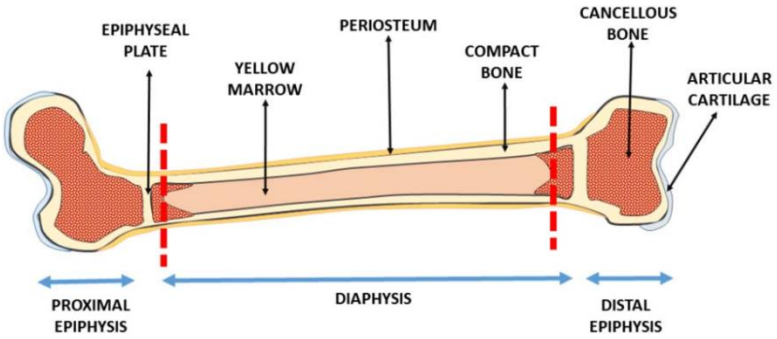

Fig. III.1 Schematic of femoral bone samples and the epiphyses structures

3.3 Experimental procedure

The employed technique is the optical noncontact and noninvasive DHI, which is described further in chapter II. The optical setup is shown in Fig. III.2 where the illumination source is a laser at 532 nm with a maximum output power of 10 W. The laser is divided using an 80:20 non-polarizing beam splitter (BS) and two single-mode optical fibers into the reference (OF1) and object beams (OF2). The BS helps to bring most of the laser beam over the bone's surface with an illumination angle of 5° with respect to the observation axis *z*. The backscattered light from the bone is collected and focused on the camera sensor by means of a lens (L) with 100 mm of focal length and a rectangular aperture (A) in front of it. A high-speed CMOS camera (PCO Dimax HD+) with 1920 × 1440 pixels at 12 bits, and working at 1000 fps, is used to acquire and record the interference pattern that is overlapped on its sensor by means of a 50:50 beam combiner (BC) in front of the camera. The field of view (FOV) of the optical system is 150 × 100 mm.

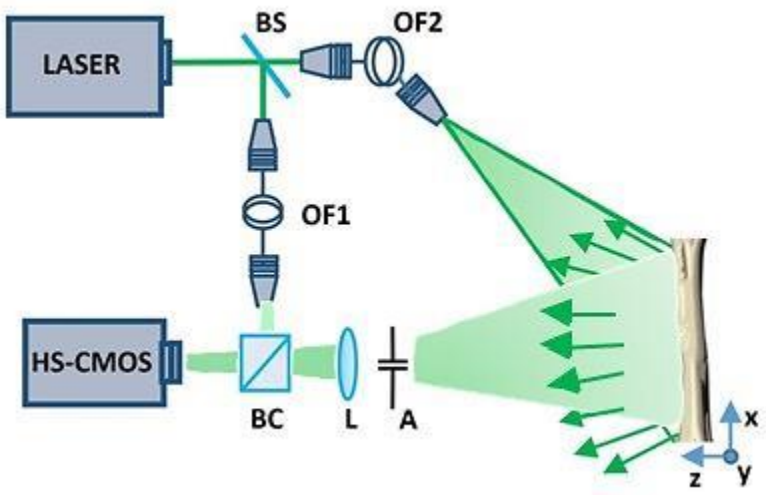

Fig. III.2. Schematic DHI optical system for Surface Structural Damage Evaluation in Cortical Bone.

As it was mentioned, the proximal and distal epiphysis in Fig. III.1 are eliminated from the sample because they conform the spongy part of the bone and thus make it impossible to have repetitive tests due their nonlinear response. Worth noting is that it is useless cutting only one post-mortem bone since it is not possible to perform several compression tests on it. (The bone's recovery mechanism is no longer available in this condition in that its structure reaches the deformation stress-strain point in their mechanical deformation behavior) [55]. For this purpose, several bones are prepared under the same conditions (<24 h post-mortem) to compress only one at a time and have the same test conditions. The femoral bones were prepared as described in section 3.2; the cutting and grinding was done with care to have parallel faces during the compression tests. These bone faces adequately match the flat supports to connect the load cell and the moving part of the mechanical press to be able to transmit the compression axially through the bone. The average length and weight for the bones were 90 mm and 55 g, respectively. The compression value is read by means of a load cell attached in series with the bone, as it is shown in Fig. III.3.

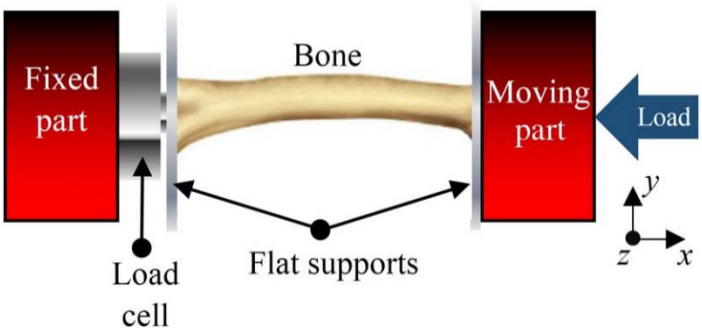

Fig. III.3. Mechanical press and load cell used to apply and read compression bone loads, respectively.

This cell helps to establish a preload value where each compression test will start, and it also registers the compression values reached. During the bone's compression, the load cell readings are stored in a computer while simultaneously the high-speed CMOS camera is recording image holograms at 1000 fps. A real-time homemade algorithm quantifies the $\Delta\varphi(x,y)$ map in Eq. (II.24) to sense the deformation presence (fringe pattern appearance) and matches each load cell value with its corresponding image in the continuous load application (the compression never stops during the image acquisition). This phase map is then unwrapped using a commercially available unwrapping algorithm (Pv_spua2 by Phase Vision Ltd.) that, as it was mentioned in chapter II, basically stitches the discontinuity jumps at $-\pi$ and π to obtain a smooth optical phase map, which is converted into a displacement map (w) with the aid of Eq. (II.19). Initially, a non-drilled bone is compressed with an axial load.

A compressive physiologic pre-charge of 30 lbs was set before each test is performed. The bone's preparation, the pre-charge value, and the fact that the load cell has a centered button for sensing, are factors that made it possible to avoid a rigid body motion in the measurements. This was proved by recording images during long periods without compression and observing the absence of fringe patterns (that otherwise would be present due to the changes in the object deformation. The

preload value was selected under the assumption of the average load range for the femoral porcine bone (see section 3.2), which is >30 lbs. Two holograms are required to calculate the optical phase for a particular compression value. The first is the corresponding hologram for the load of interest while the second has an increment of 5 lbs in load; i.e., for a compression of 50 lbs, the holograms for the 50 and 55 lb compressions are used. This load increment has the purpose to observe the surface deformation for that load value of interest, but has the same load increment (Δl) to compare among samples. Figure III.4 shows the compression values to be analyzed (30, 50, 100, 200, and 400 lbs) in a common experimental compression load curve and their corresponding Δl. Also important to mention is that the frame rate selected for acquiring the holograms (1000 fps) avoids loss of information during the continuous compression load test. The latter would be represented as uncorrelated fringes after calculation of the optical phase.

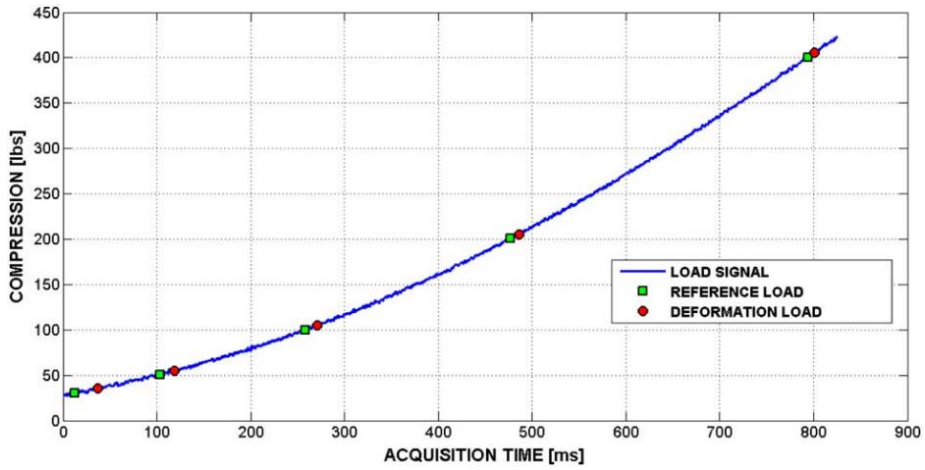

Fig. III.4. Compression values to be analyzed (green markers for 30, 50, 100, 200, and 400 lbs) and their corresponding load increment (deformation load) Δl=5 lbs during the continuous compression tests.

3.4 Non-drilled bone compression test and results.

To test the repeatability of the optical system among several samples, in this section no perforations are present over the bone's surfaces. This displacement information will be used as a reference to compare to the response of the cortical drilled bones. Several samples were compressed and analyzed in the same way, and Fig. III.5 shows the results for three different bones (left, center, and right column) at the five compression values of interest. In this figure the *x*, *y*, and *z* axes represent the length, height, and displacement, respectively (this labeling does apply to similar figures along this manuscript). From this comparison, it is possible to observe a remarkable difference between physiological loads (up to 50 lbs) and the overloads (from 100 lbs upward). The displacement observed has negative values, i.e., goes into the negative *z* direction, in the first two rows of Fig. III.5. However, these magnitudes are different in all the cases, a feature not related to the repetitiveness of the test but to the viscoelastic nature of the bone, and therefore, to its anisotropy due to its composite structure. This same behavior appears at 100, 200, and 400 lbs (third, fourth, and fifth row of Fig. III.5). Even when they show a strong trend to deform in the same direction, the magnitudes are different for each row. The bone does not show a complete isotropic response, and this is observed for any of these three samples; i.e., the bone, to a lesser extent, is still anisotropic. As can be seen between 50 and 100 lbs of compression, displacement direction is inverted due to the anisotropic response of the bone, and once it reaches a maximum displacement, about 2 μm when 100 lbs are applied, a decrease in the magnitude may be observed at 200 and 400 lbs (from 2 to 0.5 μm approximately). At this point, the viscoelastic nature of the bone is still manifested, but if the compression load continues to increase, microfractures will appear over its surface, leaving the bone unable to go back to its original dimensions. This fact indicates, in terms of the load deformation material curve [55] that the sample has left its elastic zone to enter its plastic one. As this work pursues the analysis of bones under regular loads in the process of healing, all the following

compression tests will be performed well within the elastic region of the bone, from 30 to 405 lbs. The bone under these controlled conditions shows a regular response where the cortical bone has no damage.

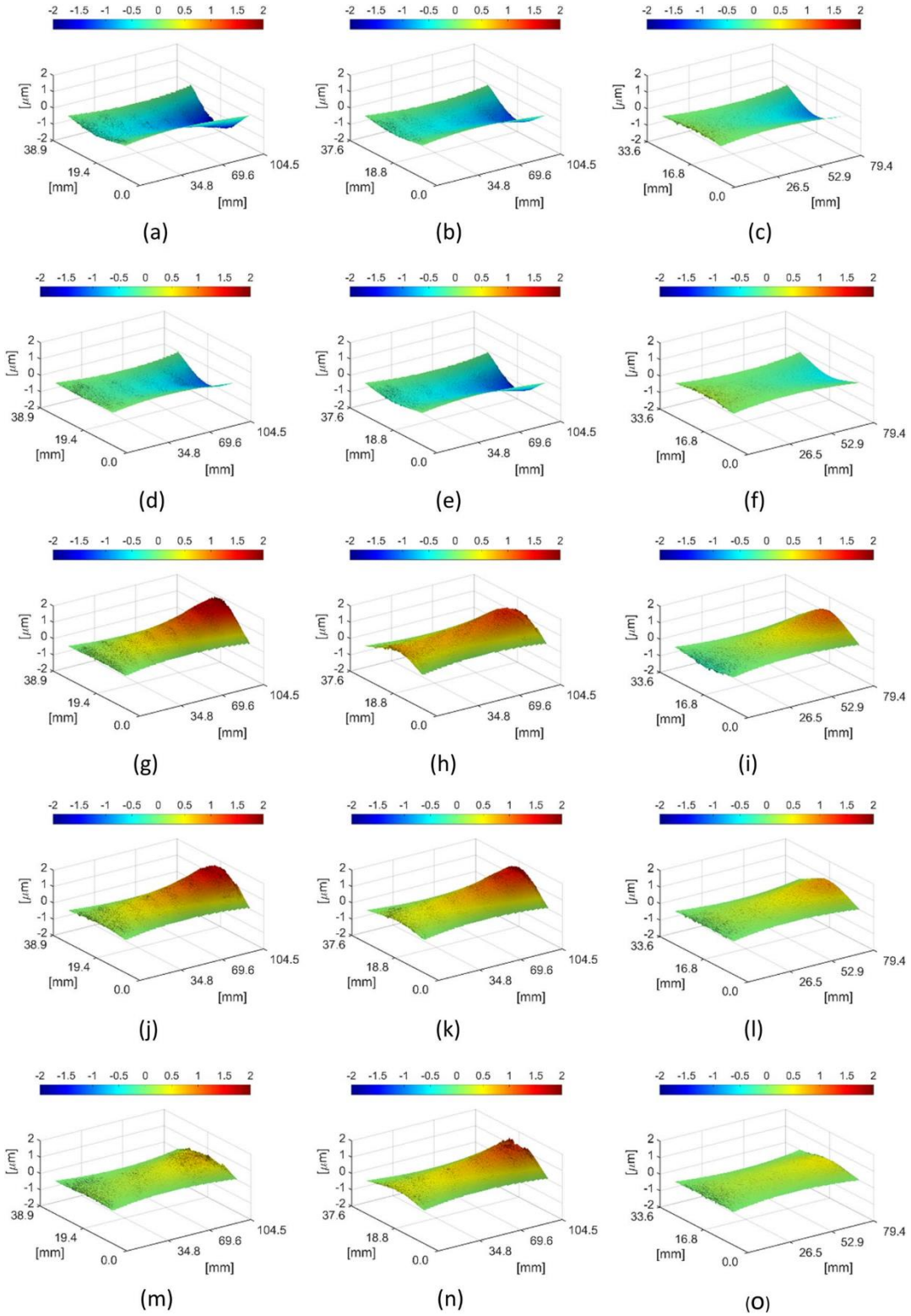

Fig. III.5. Displacement map comparison for three different non-drilled bones. Each column represents a different bone, and each row reflects the compression value of interest at (a)–(c) 30 lbs, (d)–(f) 50 lbs, (g)–(i) 100 lbs, (j)–(l) 200 lbs, and (m)–(o) 400 lbs.

3.5 Drilled bone compression test and results.

The same preload value of 30 lbs is applied when different bones are drilled with a drill bit of 4.5 mm in diameter (regular surgical diameter). Each bone is drilled with one, two, three, four, five, or six cortical perforations, and three bones are used for each perforation value, resulting in 18 samples to be analyzed. In the case of three, four, five, and six perforations, consecutive holes are separated by 12 mm on the same side of the sample, as Figs. III.6 and III.7 depict. These drilling conditions were taken from commercially available common *locked compressive plates*. For the case of two cortical perforations (samples named as 2C), the bone is drilled on opposite sides of the bone's surface, leaving one-hole side to side (Fig. III.7(b)). Similarly, four and six cortical perforations (named as 4C and 6C in Figs. III.7(d) and III.7(f)) have two and three holes on either side, respectively. The number of bones to be analyzed is reduced for simplicity because pretest results with one, two, three, four, five, or six cortical drills show that the odd number of drilling, in the unobserved side of the bone, does not modify representatively the observed optical phase with respect to previous pair numbers on the same unobserved side, as Fig. III.7 exemplifies. Very similar surface displacement is obtained with two and three drillings (Figs. III.7(b) and III.7(c) respectively), and the same occurs between four and five cortical drillings. For this reason, the tests are performed and presented with two, four, and six cortical drillings (2C, 4C, and 6C), respectively. The observation side is shown in Fig. III.2; where the side of the bone is seen by the lens aperture system and imaged on the camera sensor.

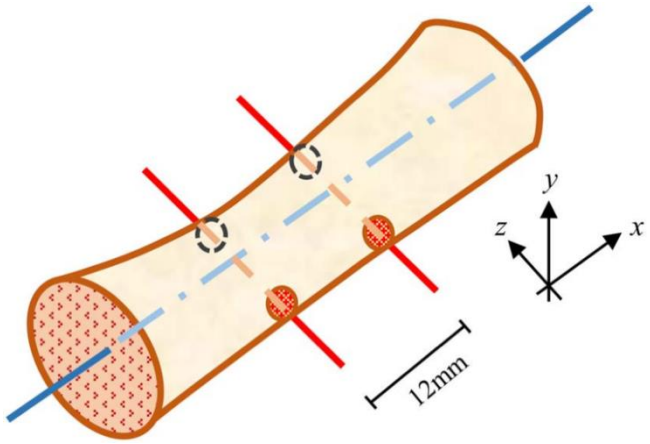

Fig.III.6. Schematic view as example for a four-cortical drilling (red axes). The drillings are performed perpendicular to the bone's longitudinal direction (blue axis)

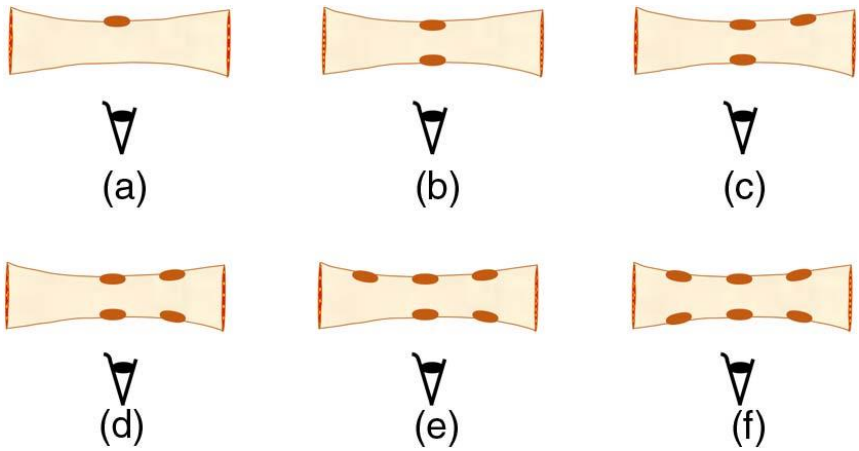

Fig.III.7. Schematic view of pretests for (a) one, (b) two, (c) three, (d) four, (e) five, and (f) six cortical drillings, where the observation side is indicated.

In Fig. III.8, the surface displacements from nine different bones are presented. These samples were drilled using a 4.5 mm drill bit diameter and compressed from 30 to 35 lbs to observe how the displacement's profile changes at the same load due to the loss of bone volume in a physiological load region.

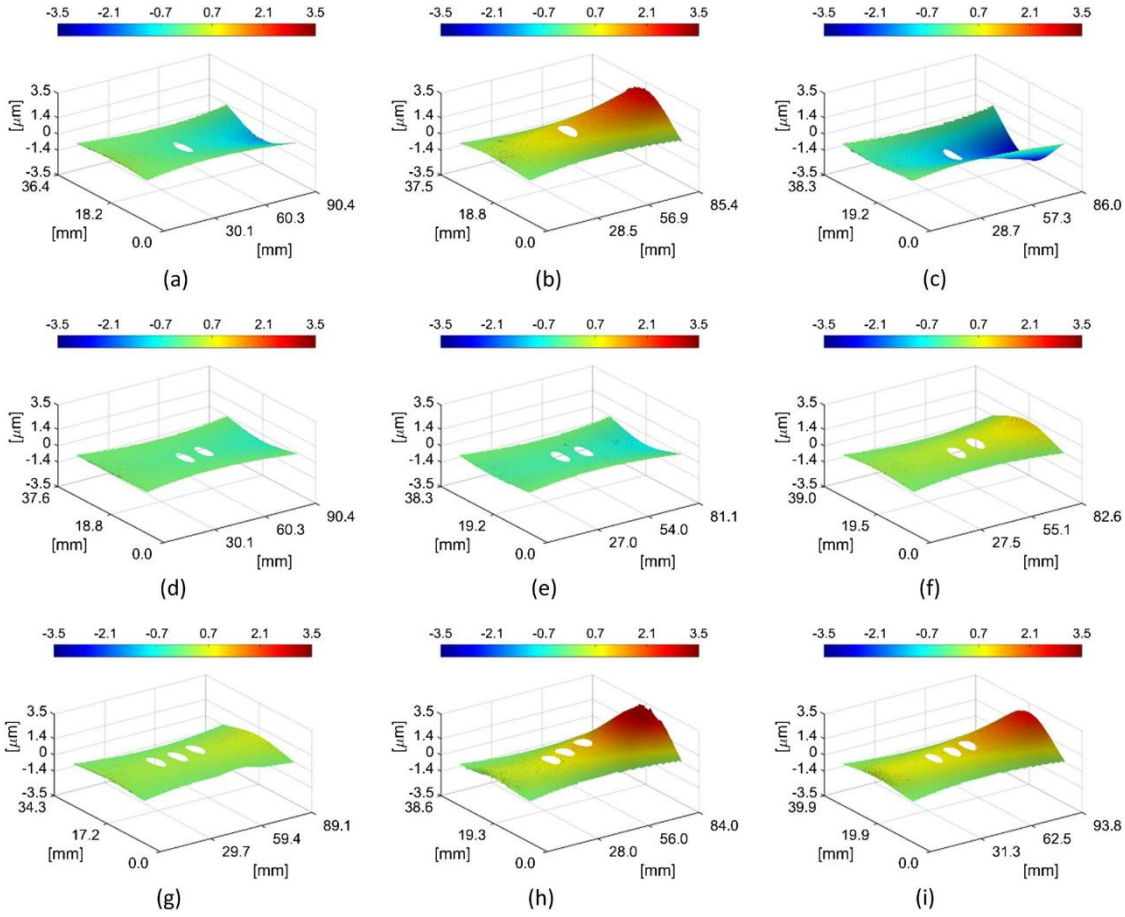

Fig. III.8. Displacement maps comparison for nine different samples with (a)–(c) 2C, (d)–(f) 4C, and (g)–(i) 6C, all at 30 lbs.

As the number of drillings grows, the displacement magnitudes reach higher values due to the re-arrangement of the bone; this shows how the bone's volume loss makes the response of the bone under the compression load more complex, which represents a weakening in the bone structure, a feature also observed at 50 lbs in Fig. III.9. These displacement magnitudes are much less consistent compared to those of the nondrilled bones (Fig. III.5). The bone's surface displacements do not tend to occur in the same direction, and the maximum displacement magnitudes are increased (along the positive and negative z axis).

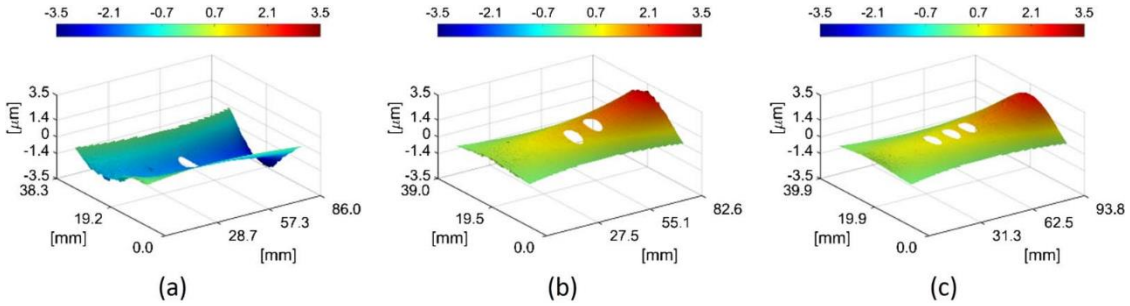

Fig. III.9. Displacement profile for three bones with (a) 2C, (b) 4C, and (c) 6C at 50 lbs.

To complete the overload designed region, a test using nine bones with 2C, 4C, and 6C at 100, 200, and 400 lbs is performed. The representative retrieved surface displacement maps by three different samples are shown in Fig. III.10. The 2C drilling results in this figure show a similar response as those observed in Figs. III.8 and III.9 while 6C drillings show a magnitude reduction when the compression reaches 400 lbs. An opposite behavior is observed with 4C drillings where the displacement magnitude is increasing with the compression. Then there should be a relationship between the anisotropy of the bone and the number of drillings or loss bone volume that makes it less viscoelastic at high compression values.

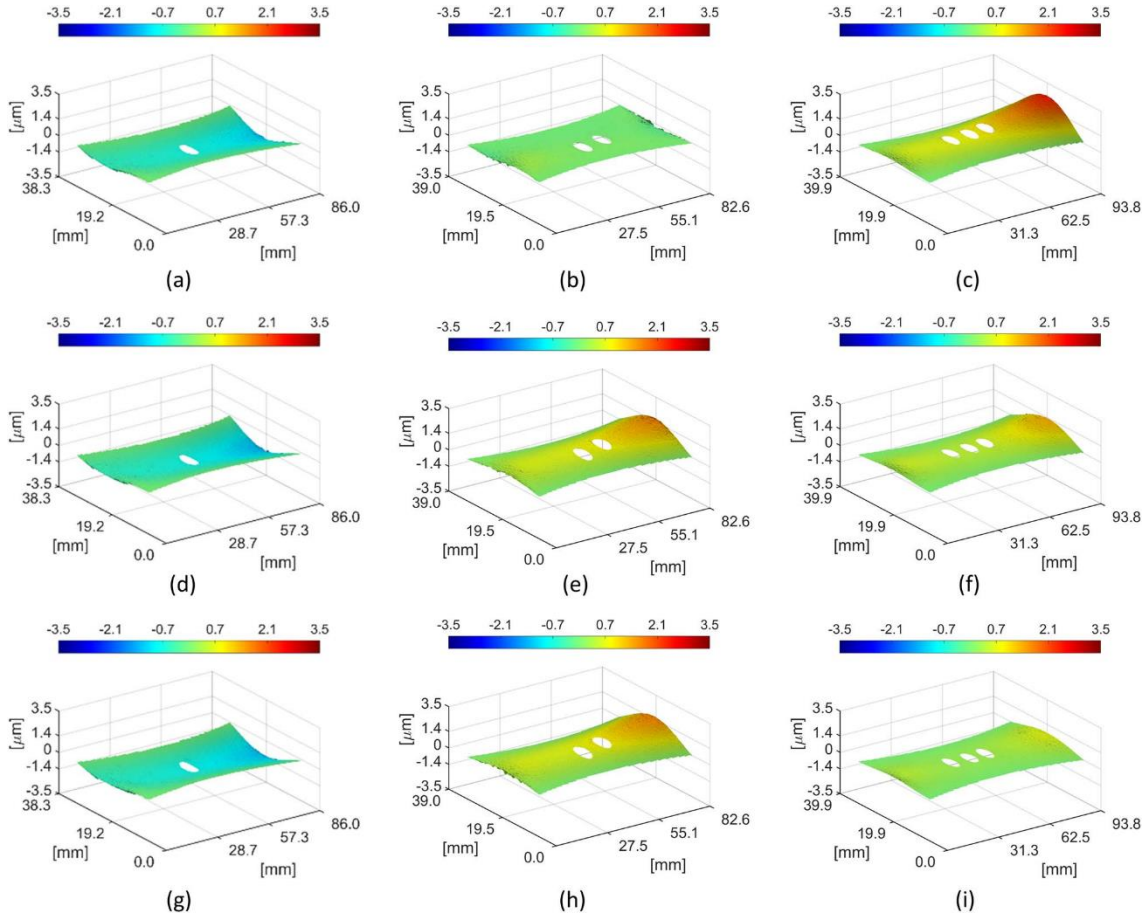

Fig.III.10. Retrieved displacement maps for three bones with 2C, 4C, and 6C at (a)–(c) 100 lbs, (d)–(f) 200 lbs, and (g)–(i) 400 lbs. Each column represents a different bone.

To have a wider comparison, a similar analysis is performed on new bone samples with 2C, 4C, and 6C, but this time they are all drilled with a drill bit of 6.5 mm in diameter (also a surgical screw diameter). Results for 50, 100, 200, and 400 lbs of compression are presented in Fig. III.11. From this figure, it is possible to observe a high surface displacement at low compression values (Figs. III.11(a), III.11(b), and III.11(c)) where the anisotropic nature of the bone is present. The maximum displacement magnitudes at 50 lbs are greater than those registered in Fig. III.9, with the drill bit of 4.5 mm (4 μm compared to 3 μm). At higher compression loads the bone's surface displacement is smaller than their corresponding value at 4.5 mm (Fig. III.10). Comparing Figs. III.9,

III.10, and III.11, notice that lower compression values and fewer drillings create higher surface displacements while higher compression values and more drillings result in smaller surface displacements. The latter is a particular behavior for a composite material with viscoelastic properties such as the bone. The bone's volume loss increases the stiffness of the bone and decreases its rearrangement capability for creating small displacements with higher strain concentrations. This creates a more fragile structure that cannot modify itself during a compression, and microfractures start to take place until a large fracture appears.

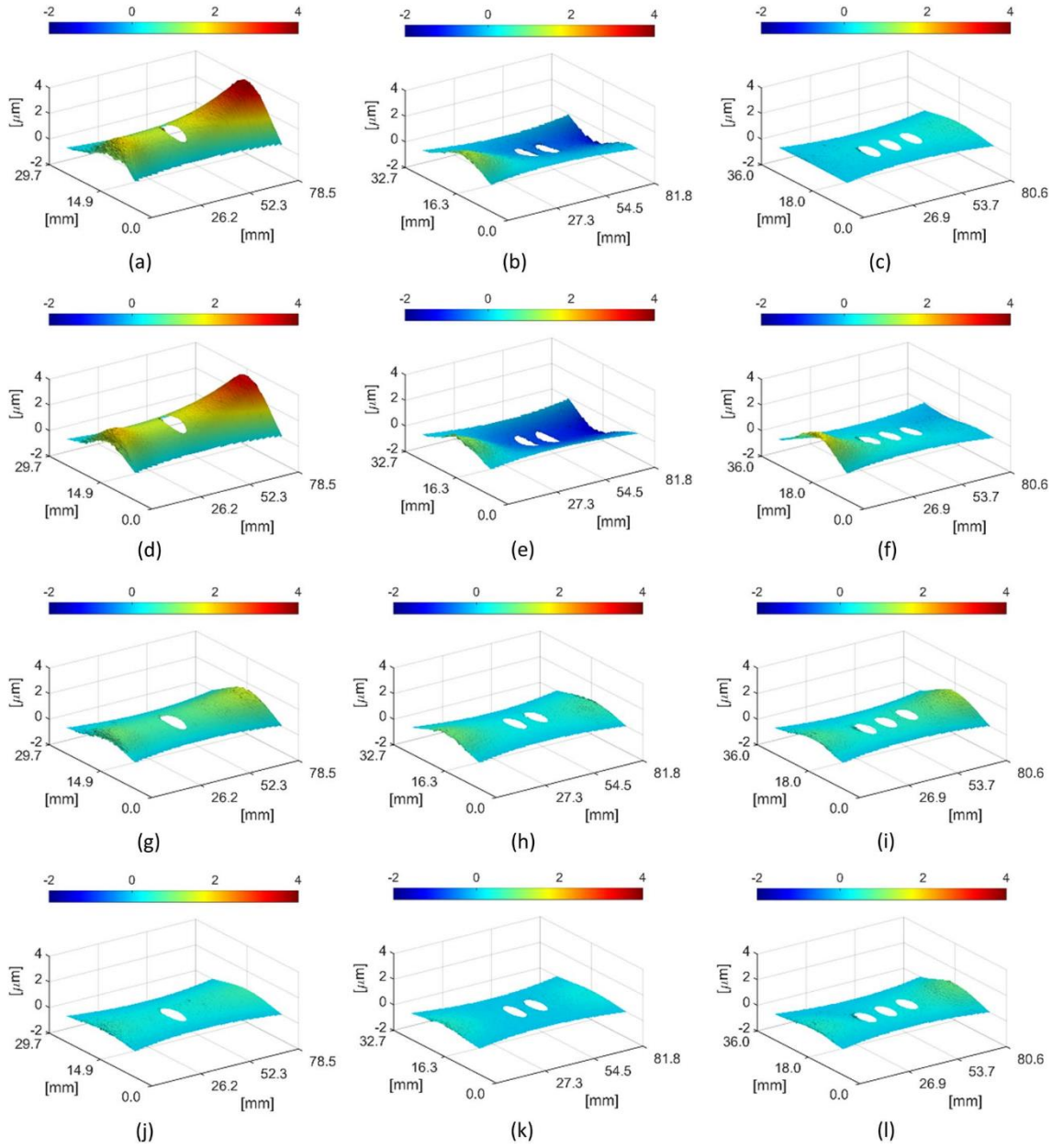

Fig.III.11. Retrieved displacement maps for three bones with 2C, 4C, and 6C at (a)–(c) 50 lbs, (d)–(f) 100 lbs, (g)-(i) 200 lbs, and (j)–(l) 400 lbs for a 6.5 mm diameter drill bit.

In Fig. III.12 a central profile comparison is presented for 6C bones with 4.5 and 6.5 mm drillings, and the average profile of the non-drilled bones at 200 lbs. This comparison shows how the bone loses its capability to deform at high compression values when the diameter of the holes is increased. The profile of 6C with 6.5 mm shows a break near the edge of the first cortical drill (orange circle in Fig. III.12), indicating the beginning of microfractures around the hole, which in turn, lead to the loosening or misalignment of the prosthetic fixation.

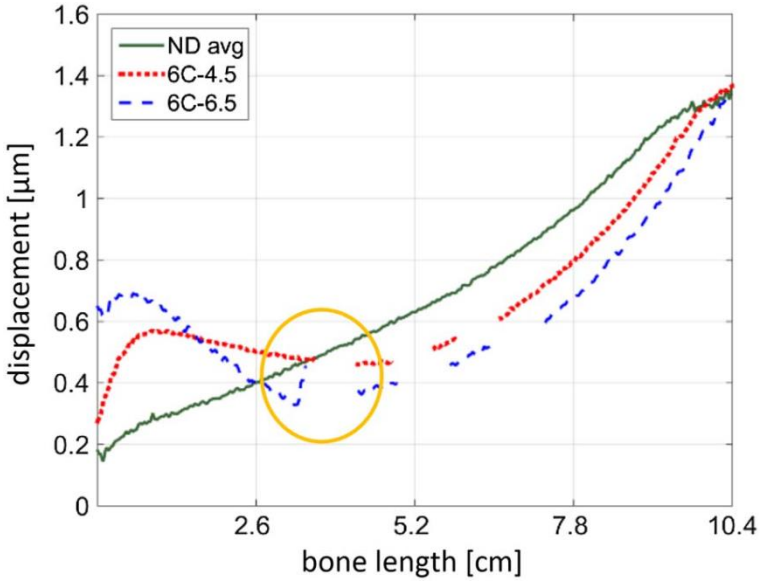

Fig. III.12. Profile comparison at 200 lbs and 6C drillings with drill bits of 4.5 and 6.5 mm compared to the nondrilled average profile. Discontinuities in the red and blue profiles represent the space due to the drilling

IV. HOLOGRAPHIC INTERFEROMETRIC SYSTEM FOR STUDY OF CORTICAL BONE QUALITY AFFECTATIONS AND THEIR STRENGTH IMPACT.

In the previous chapter it was found, in terms of surface displacements, a particular relationship between the volume of the cortical bone structure and the quantity of load that the sample undergoes. The latter can be stated as: “For low load and more bone volume, the bone structure is more deformable. Less bone volume and more load limit the deformable range of the bone structure”; which is an amazing property attributable indeed to the particular composite of cortical bone structure and contrary to simple materials when more volume absence increase the range of deformations that they undergo. The present chapter aims to unveil the dynamics in bone strength when its composition is altered in a controllable way and how this condition affects healthy bone conditions.

4.1. Introduction.

According to the American Association of Clinical Endocrinologists (AACE), osteoporosis is defined as a condition characterized by a low bone mass. Under this affectation, the micro architectural deterioration of the bone tissue leads to bone fragility and increases the probability to suffer a fracture [56]. As it was mentioned previously, the bone structure is biphasic, meaning that there is an organic matrix and an inorganic mineral component in it. The three primary constituent elements of the bone are: (1) fibrillary type 1 collagen (35 to 45% of the volume), (2) mineral linking of calcium-phosphate (35 to 45% of the volume) in the form of semi-crystalline hydroxyapatite, and (3) water (15 to 25% of the volume) [28-29]. As a person ages, his/her bone's susceptibility to fracture increases, however, it has been shown that there is no change in the bone’s mineralization with aging,

but bone becomes less tough without a direct answer for the question, what elements in bone change then? [57]. The aging effect and the bone's risk to fracture are therefore related to the organic phase and to the inorganic part. The property of the bone to resist fractures is known as strength [58], recently described as a complex concept determined by the integration of three factors: quantity, quality and turnover of the bone [32]. The quantity is generally related to bone density, mineral and collagen content, although common clinical procedures focus just on the mineral amount. The bone quality depends on the structural and material properties of the bone. The structural properties include its geometry (size and shape) and microarchitecture. The material properties include the organization and composition of the mineral and collagen components of the extracellular matrix [32]. On the other hand, the bone turnover is related to a metabolic response which allows a continuous renewal of the tissue by means of a resorption and formation processes. The balance between resorption and formation helps the bone to remove fatigue damage and replace it with new bone that reinforces its integrity. Since an imbalance between the resorption and formation results either in a loss or gain of bone, the turnover process affects the bone quantity and the bone quality, and as consequence, affects the bone strength [32], [58].

The bone mineral density (BMD) is a clinical rating based on the dual energy X-ray absorptiometry technique (DXA) which obtains relative values of the bone quantity. A common practice is to express the BMD in terms of the so-called T-score. The latter reports the number of standard deviations for a patient's BMD value compared to a reference BMD value for a healthy 30-year-old adult of the same gender and similar ethnic group [59-60]. Even though the BMD value is used for medical practitioners to assess the risk of fracture, it has been found that less than 50% of the whole bone strength is attributable to its variations [61-63]. As a matter of fact, the majority of patients who experience fragility fractures have a BMD T-score above -2.5. If we consider that a normal bone density is above -1.0 and osteoporosis is below -2.5, those patients are medically

diagnosed with osteopenia (low bone density); it means that although their bones reveal a BMD loss, they could never develop osteoporosis [64-66]. Another argument deals with the hip fracture probability which is five times greater at the age of 80 than at the age of 50 in women with a T-score of -2.5, [66]. This means that hip fractures in elderly population are produced by many factors which are not necessarily correlated to the mineral bone mass loss caused by osteoporosis.

Furthermore, BMD value is limited to diagnose the secondary causes (conditions besides osteoporosis) of bone loss and to assess the response to a therapy. Then, the other two determinants of the bone strength: *quality* and *turnover*, should be included when assessing fracture risk in each individual rather than just the BMD score alone [67]. As a consequence, nowadays osteoporosis disease has been re-defined as "a skeletal disorder characterized by compromised bone strength leading to an increased risk of fracture" [68]. This definition implies that understanding the bone strength may be the key to better understand the fracture risks [58].

In this chapter the effects of secondary affectations to the bone structure strength are analyzed in terms of its surface displacements. The objective of this study is to use an optical non-destructive technique to retrieve high resolution full-field information of the bone samples in order to estimate the impact of different affectations in their mechanical response (strength). This optical non-destructive testing (NDT) called digital holographic interferometry (DHI) is applied in ex-vivo samples [13], [69] in order to gain new knowledge to eventually complement diagnoses related to bone strength evaluation beyond those obtained by BMD score. The study includes structural affectations to the bone obtained by degrading one or more of their principal components: hydroxyapatite, collagen and water. The cortical bone probes are observed with DHI in an out-of-plane sensitivity set up, while a testing machine applies a controlled compression load. The out-of-plane sensitivity was selected considering that its magnitude is much greater than the in-plane one in

cortical bone [69] (the mechanical response of the bone is mostly expressed). This configuration has the advantage to record the surface deformation information during the entire test (dynamic test) without the need to remove the samples to analyze them (static test). In addition, the interferometer registers full-field information over the entire object's surface, a feature required due the bone's anisotropy. A precise characterization of the affectation procedures was carried out before each compression test was performed. Once characterized, a displacement comparison for each affected group is presented.

4.1.1 Bone Affectation classification.

There are several conditions and diseases that directly and indirectly affect bone quality rather than just osteoporosis (secondary affectations) which have been reported [32], [58], [70]. These disorders were categorized considering about 20 different conditions/diseases affecting bone quality [67] as follows:

Disorders of bone mineral homeostasis.

Bone mineralization is one of the major determinants of the bone quality and it is controlled by the mineral homeostasis process. Any possible condition that may interfere with the mineral homeostasis will affect the bone quality (leading to a fragility fracture) [32]. Patients who present an affectation to the mineral homeostasis are normally supplemented with an adequate calcium and vitamin D intake since these components are relevant to the bone mineralization [32], [67] however, their mineral quality could be compromised if their remodeling process is affected by an abnormal homeostasis process.

Imbalance of the bone remodeling

Some bone diseases such as osteodystrophy or disuse osteoporosis are caused by a high turnover state which provokes an increased activity of the osteoclasts [71-73]. As a consequence, the bone remodeling process is shifted towards the bone resorption, resulting in an imbalance of the bone turnover that causes fragility fracture. Moreover, if the defect is related to the osteoclast function such as osteoporosis, this could lead to a lack of bone heterogeneity, micro-damage accumulation and, consequently, fragility fracture [74-75].

Collagen disorders

Type I collagen makes up approximately 95% of the organic matrix found in the bone. The collagen helices are crosslinked in between (increasing their strength). At the same time, this crosslinked collagen pattern forms a structural template for the bone mineralization [76]. This composition between collagen and mineral gives the bone its remarkable material properties. The bone strength and stiffness depend heavily on the mineral content [77-79], while the collagen plays a role in the bone structural integrity giving its tensile strength [80-82]. Usually the bone fails in tension, but collagen provides the main structural framework to prevent this failure. This is a paramount reason why a disruption of the collagen structure causes bone fragility (as it happens in osteogenesis imperfecta).

Drugs affecting bone quality

Some medications can bring a great therapeutic benefit; however, they normally involve collateral effects. Medications taken for the treatment of arthritis and psychotropic and epileptic disorders, as well as anticoagulants, antacids, bisphosphonates, corticosteroids, and antineoplastic drugs, can profoundly affect bone metabolism. In some scenarios (eg, osteoporosis), these effects are

intended; in others (eg, rickets, osteomalacia secondary to antiepileptic drugs), potentially adverse side effects of medications on bone may occur. Nonsteroidal anti-inflammatory drugs appear to delay fracture healing and bone ingrowth, although these effects are reversible. [83-86].

4.2 Method

4.2.1 Bone sample preparation

In order to study the bone strength, cortical bovine bone samples were treated by means of demineralization [87-89] and air-drying [90-93] protocols, to affect the mineral and organic phases respectively. These procedures will represent bone quality and quantity affectations as the bone turnover affectation is caused by affecting one or both of them. It is worth mention that these protocols are independent from each other, i.e., the demineralization process does not affect the air-drying process and vice versa. The bovine femur bones were obtained locally with less than 24 hrs post-mortem and all of them come from male bovine strain Angus, which are regular sized with an average weight of 1000 kg and bred for human consumption. The slaughter age of the cattle was approximately 20 months. These cortical bovine femur samples were obtained from the middle diaphysis by hand saw avoiding the use of electric devices which induce heat. The average mean transverse section of the diaphysis is 1960 mm^2. All these femoral diaphyses were submerged in spring water for about 90 minutes to easily clean out other tissues by using a scalpel. After that, a low speed rotating diamond wheel saw was used, the cortical samples were carefully machined to a prismatic geometry of 5 × 5 × 17 mm as seen in Fig. IV.1. The longest length of the samples (b = 17 mm) was selected to be aligned to the growth direction of the bone. The transverse section (a × a, 5 × 5 mm) of the final samples was selected considering the temporal model for the demineralization process which acts in a radial form going from the periphery towards the center [89], [94-97].

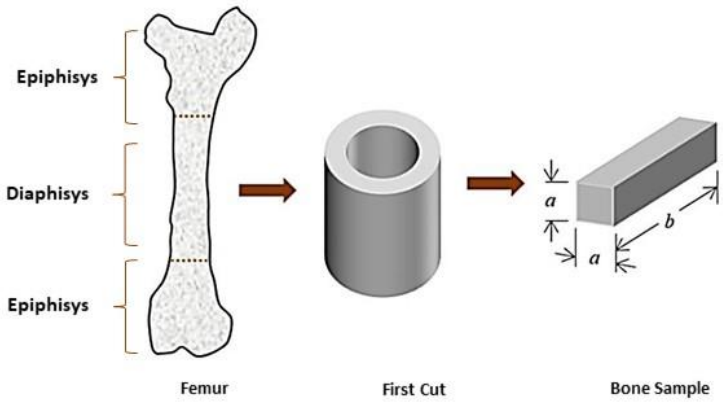

Fig IV.1. Schematic of the cortical bovine bone samples machining steps. Opposite faces of the bone samples are parallel.

It is important to point out that before, during and after the entire machining process, the samples were kept fresh and wet using a 0.1 M phosphate-buffered saline solution (isotonic substance to preserve cellular tissues due to its osmolality). Even when the rotating diamond wheel machine was used, the bone samples were always irrigated with this solution. Once machined, they were grouped into four groups, shown in Fig. IV.2.

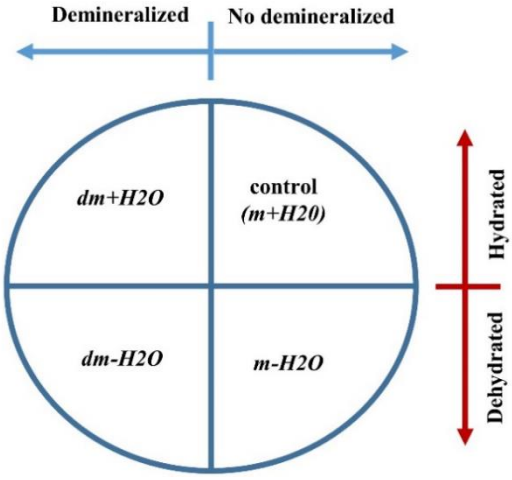

Fig. IV.2. Bone sample groups to be tested.

The control group *(m + H2O)* kept its normal mineral and hydration contents. The hydrated but demineralized group *(dm + H2O)* was divided into two subgroups; one of them was demineralized for 4 hrs and the other for 6 hrs in order to check the demineralization process effect. In a similar way, the mineralized but dehydrated group *(m-H2O)* has two subgroups too: one is air-dried during 24 hrs and the other one during 48 hrs. The fourth group is dedicated to demineralized and dehydrated samples for 48 hrs *(dm-H2O)* with two demineralization subgroups of 4 and 6 hrs for control purposes. In order to verify the affectation of collagen, hydroxyapatite and water produced by the demineralization and air-drying protocols, a total of 24 cortical samples were tested using the Fourier transform infrared spectroscopy (FTIR) technique as will be shown in section 4.3.1.

4.2.2 Demineralization process

The bone is a composite material hierarchically structured and there are two types of it: cancellous and cortical. Both types are conformed by type I collagen fibrils containing mineral (hydroxyapatite) sparsed allong them [77], [97-101]. This organic and inorganic composition requires treating the bone samples with a demineralization method that affects only the inorganic mineral component while the organic component is preserved. Bone demineralization studies based on Hydrochloric Acid (HCl) have shown a geometric dependence among the samples. The HCl solution penetration distance is a function of the square root of the time employed, giving a control of the cortical and cancellous bone demineralization while the collagen is preserved [87-88]. The in vitro demineralization method applied in this work has remarkable characteristics. The rate of demineralization increases according to the HCl solution concentration and temperature. The bone demineralization has three stages; in the first one, the constant demineralization rate increases as the HCl solution demineralizes the peripheral region of the sample. The second stage occurs on a steady state and the third one at the end of the reaction when the constant rate decreases [89]. In order to check the demineralization method and its effects on the bone strength, two demineralizing times

were employed, 4 and 6 hours. Each cortical sample was placed in a 50 ml clinic beaker containing 40 ml of 0.6N HCl at room temperature (21°C). According to the method's protocol [89], the HCl solutions were renewed for the samples after 0.5, 1.5 and 3 hours until 4 and 6 hours of demineralization were reached. The HCl solution parameters (concentration and temperature) were carefully selected to avoid changes in the final dimensions of the bone. The increase of these parameters is not recommended for mechanical tests because the bone final structure and dimensions are deeply compromised.

4.2.3 Dehydration method and its collagen affectation

Removing the water present in the bone by an air-drying method represents a process that has been previously employed in order to analyze bone structure at different scales [90-91]. Room temperature and dehydration periods of 24 and 48 hours were applied. Water conforms about 20% of the bone's volume and it is a key factor for the mechanical behavior of the bone. It is found basically in two parts: within the pores and bounded to the matrix where it is responsible for giving the collagen its ability to give the bone's ductility or plasticity [90]. Thus, affecting the bound water level results in a collagen affectation and, as a consequence, the natural structural bone response is altered. This dehydration method has been employed in different bone samples such as bovine, porcine, equine, human tibia, femur and humerus [91-93].

4.3. Experimental Procedure.

4.3.1 Fourier transform infrared spectroscopy (FT-IR) validation

At this stage of the study, electromagnetic radiation corresponding to the infrared band (400 to 4000 cm-1) is directed onto the sample. The energy associated with these wavelengths is absorbed by the bone and converted into molecular vibration energy depending highly on the chemical groups

present in the sample, thereby demonstrating their chemical structure. Many FT-IR studies have been made on bone identifying characteristic bands for mineral matrix groupings in hydroxyapatite at 500 - 700 cm-1 and 900 - 1200 cm-1; the organic matrix (collagen) in the 1200 - 1700 cm-1, and also for bound and pore water molecules in 3427 cm-1 [102-103].

In order to prove qualitatively the effect of bone demineralization and collagen affectation protocols, a Cary 670 FT-IR system was employed to test cortical samples with the specified geometry shown in Fig. IV.1. The samples were grouped as it was described in section 4.2.1 (Fig. IV.2) and each of them was transversally sectioned and observed in several points within the transverse section. The FT-IR spectroscopic system obtains each spectral value with 32 repetitions per sample and its analysis is necessary to guarantee that samples under compression are independently affected in the mineral, collagen and water components. Figure IV.3 depicts a comparison among the mean spectral transmittance for samples with 4 and 6 hours of demineralization *(dm + H2O)* with respect to the control samples *(m + H2O)*. In this case, all samples did not go through an air-drying treatment previous to the FT-IR test. From Fig. IV.3 it is possible to observe signals at the bands of the hydroxyapatite (1010 cm-1), collagen (1600 cm-1) and water (3427 cm-1) [102-103]. It can be seen that the transmittance percent of the band at 3427 cm-1 for water is almost the same for 4 and 6 hours, hence it is safe to assume that water content tends to be the same independently of the demineralization time.

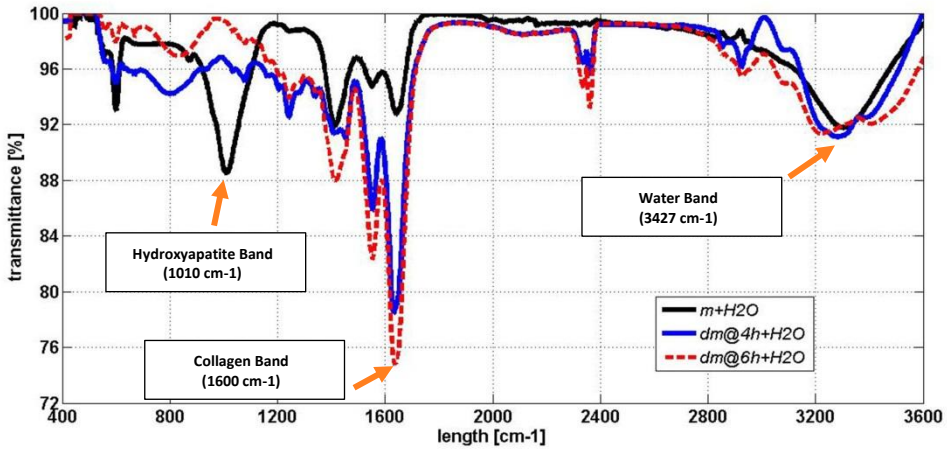

Fig. IV.3. FT-IR mean transmittance spectra comparison for samples with 4 (blue continuous line) and 6 (red dotted line) hours of demineralization (dm + H2O) with respect to the control group (m + H2O).

For each spectrum, Table IV.1 shows the transmittance percent ratio values between the three components hydroxyapatite (H), collagen (C) and water (W) for each group. The transmittance ratios of the hydroxyapatite with respect of the collagen has increased from the control group $R_{HC} = 0.95$ to *1.22* and *1.33* for 4 and 6 hours of demineralization respectively (i.e., to obtain $R_{HC} = 0.95$ for the control group it was divided its hydroxyapatite transmittance value of *88.5*, by its corresponding collagen transmittance value of *93* according to information of Fig. IV.3). This means that in the bone sample the relative ratio of collagen increases, while the ratio of hydroxyapatite decreases as result of the bone demineralization and the corresponding ratio is greater when the time is larger.

Table IV.1. **Transmittance ratios R_{HC} (hydroxyapatite/collagen) R_{HW} (hydroxyapatite / water) R_{CW} (collagen / water) considering the bands of hydroxyapatite (1010 cm−1), collagen (1600 cm−1) and water (3427 cm−1) for the control and demineralization process spectra shown in Fig. IV.3.**

	Transmittance ratios		
Bone Sample Group	R_{HC}	R_{HW}	R_{CW}
m + H2O	0.95	0.96	1.01
dm@4h + H2O	1.22	1.04	0.85
dm@6h + H2O	1.33	1.08	0.81

Similarly, the dehydrated samples (m-H2O) are analyzed using the FT-IR technique and Fig. IV.4 shows their corresponding transmittance spectra. In this case the two subgroups of 24 and 48 hours of dehydration are compared. As in Fig. IV.3, the transmittance bands of the hydroxyapatite, collagen and water are observed [102-103]. The transmittance ratios among these bands are shown in Table IV.2 and it is possible to observe that the relative proportion of collagen is reduced as the time increases. RHC is reduced from 0.95 of the control group to 0.90 and 0.89 for 24 and 48 hours of air-drying respectively. Analyzing further these ratios, it can be observed that the content of water has been reduced drastically as RHW from the control group was 0.96 and it is reduced to 0.88 for both 24 and 48 hours (see Table IV.2). Since there is no difference between the two air-dried samples, for convenience the samples at 48 hours are used in the compression tests.

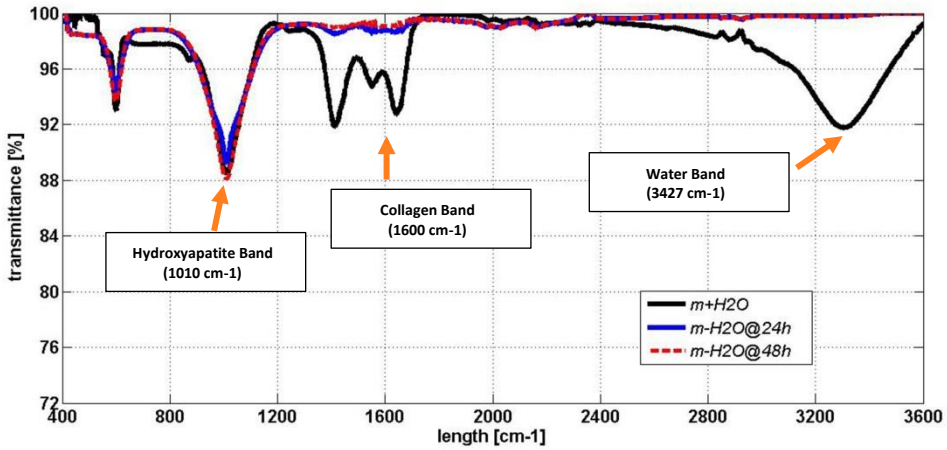

Fig.IV.4. FT-IR mean transmittance spectra comparison for samples with 24(blue continuous line) and 48(red dotted line) hours of air-drying (m-H2O) with respect to the control group (m + H2O).

Table IV.2. **Transmittance ratios R_{HC} (hydroxyapatite/collagen) R_{HW} (hydroxyapatite / water) R_{CW} (collagen / water) considering the bands of hydroxyapatite (1010 cm−1), collagen (1600 cm−1) and water (3427 cm−1) for the control and air-drying process spectra shown in Fig.IV.4.**

	Transmittance ratios		
Bone Sample Group	R_{HC}	R_{HW}	R_{CW}
m + H2O	0.95	0.96	1.01
m-H2O@24h	0.90	0.88	0.98
m-H2O@48h	0.89	0.88	0.99

4.3.2 Compression tests

Once the FT-IR spectroscopic signals were analyzed to validate the affectation processes on the bone samples, the selected groups were compressed in order to register their temporal behavior during this controlled compression tests. The load values to be compared are 100, 200 and 300 lbs because they represent load stages for the samples which include physiological (100 lbs) and overload conditions (200 and 300 lbs). The maximum compression load represents more than 40 times the normal load value considering mean weight and femoral transverse section of the selected cattle scaled to the area of the machined bone samples (section 4.2.1). The groups tested are: *m+H2O*

(control), dm@4hrs+H2O, dm@4hrs-H2O@48hrs and m-H2O@48hrs. Figure IV.5 shows the average temporal response comparison of several affected samples for each cortical sample group during a full compression test.

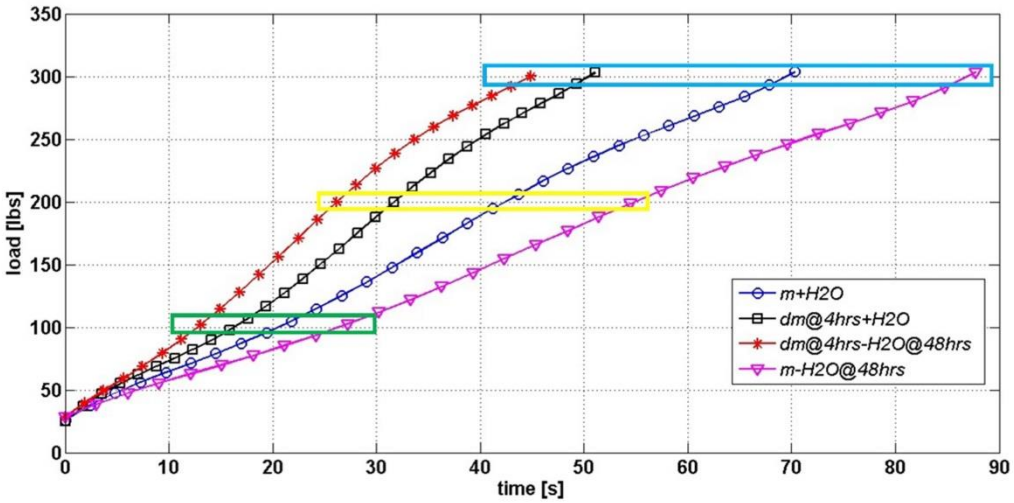

Fig. IV.5. Mean temporal response for each cortical sample group with region marker for 100 (green), 200 (yellow) and 300 lbs (blue).

Considering the control group *(m+H2O)* as a division parameter, two regions are observed in Fig. IV.5, one at the top and the other at the bottom. Samples which are air-dried *(m-H2O@48hrs)* show an opposition to the compression movement and they are located at the bottom region because more time is needed to reach the final load of 300 lbs under a linear temporal compressive profile respect to *m+H2O*. Table IV.3 shows that this air-dried group has time delays corresponding to 7, 12.2 and 17.5 seconds for loads of 100, 200 and 300 lbs respectively, as compared to samples with normal conditions of hydration and mineralization *(m+H2O)*. Observing this behavior, it may be thought that the *(m-H2O@48hrs)* group presents more strength, but in fact as they have lessened their collagen volume their stiffness increases. In other words, they become more fragile in terms of the mechanical stress-distension material curve [104]. The latter results in a linear response that may fail or break suddenly before they experience any permanent deformation (e.g., brittle like a crystal) [77]. On the other hand, at the top region, groups appear which are treated for demineralization with

and without air-drying procedure *dm@4hrs+H2O* and *dm@4hrs-H2O@48hrs*. As the inorganic mineral structure provides the bones with a mechanical support, the lack of it is clearly observed by the time required for these samples to reach the final load value which is smaller with respect to *m + H2O* (Table IV.3). The opposition against the compression movement is diminished in the demineralized groups and they start to behave predominantly malleable due to the collagen nature even when it is also affected, especially in dm@4hrs-H2O@48hrs. In terms of the stress-distension curve, the bones are more flexible and they could be deformed considerably before a failure or break appears [105]. The latter is not a desirable condition because they lack of any mechanically stable morphism.

Table IV.3. Temporal comparison among sample groups.

Load	**Time to reach the selected load value (sec.)**			
(lbs)	***m-H2O@48hrs***	***m + H2O***	***dm@4hrs + H2O***	***dm@4hrs-H2O@48hrs***
100	27.1	20.1	16	13
200	54.4	42.2	31.7	26.2
300	87.6	70.1	50.2	44.9

4.3.3 Opto-mechanical system measurement and surface displacements results

The schematic view of the DHI system is shown in Fig. IV. 6 where the illumination source is a *Verdi* continuous wave (cw) laser at $\lambda = 532$ nm. This laser beam is divided using an 80:20 non polarizing beam splitter (BS), into the reference (OF1) and object (OF2) beams. These beams are conveyed and delivered by means of single mode optical fibers. The BS helps to bring most of the laser beam over the bone's surface with an illumination angle of 5° with respect to the observation axis z. The backscattered light coming from the bone's surface is collected and focused on the camera sensor by means of a lens (L) with 100 mm of focal length and a rectangular aperture (A) in front of it. A high-speed CMOS camera (PCO Dimax HD+) with 1920 × 1440 pixels at 12 bits dynamic

range (bit-depth), working at 1000 frames per second (fps) is used to acquire and record the interference pattern coming from the overlapping of the reference and the object beams using a 50:50 beam combiner (BC) placed in front of the camera. The observed area of this optical arrangement is set to 20 × 20 mm which covers the entire bone sample dimensions. The cortical samples were prepared as it was described in section 4.2.1 and their flat and parallel faces adequately match the flat supports of a micro compression testing machine (MCTM) which was specifically designed and built for optical non-destructive testing. This testing machine gives the opportunity to analyze and compare the different bone responses in the same experimental load conditions.

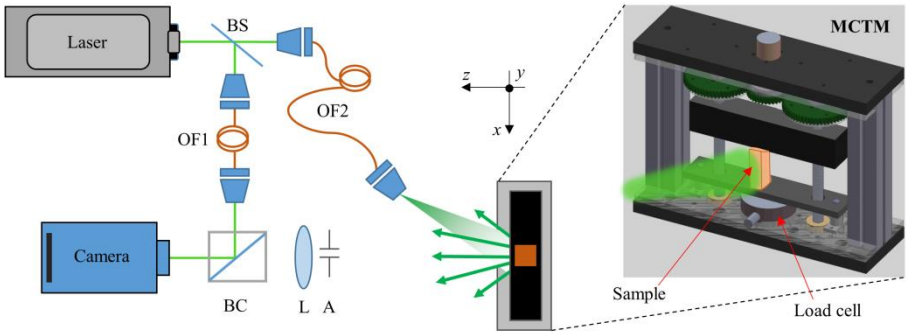

Fig IV. 6 DHI set up for the cortical bone compression tests.

The MCTM compresses each sample axially with a load range which covers from 0 up to 300 lbs and as it was mentioned previously, the maximum load will represent an overload of up to 40 times with respect to their normal value (overloads in bone are practically considered from about 10 times with respect to their physiological load) [104]. It is important to mention that the MCTM was previously calibrated under standard compression tests using known material samples (aluminum 6061) with extension gauges sensors attached to them. The embedded control design of the MCTM allows a linear compression using a close loop method which is a relevant feature because it differentiates a non-linear structural response of the bone from the compression signal. The

compression value is read by means of a load cell fixed at the bottom of the MCTM and helps to set the same preload value for each compression test. During the compression test the load cell readings are stored in a computer while simultaneously the high-speed CMOS camera is recording image holograms at 1000 fps. A homemade algorithm matches each load cell value with its corresponding image hologram in the continuous load application (the compression never stops during the image acquisition). The procedure to place each sample before the compression tests starts by placing the bone probe over the bottom support of the MCTM in front of the optical system. After that, the bone sample is compressed to a preload value of 30 lbs which simulates a physiological value. The machined bone's parallel faces and the preload value avoid rigid body motion in the measurements. The latter was proven by recording images during long periods with just the preload compression and observing the absence of any fringe patterns. As two image holograms are required to calculate a displacement map, the selected compression load uses the corresponding image hologram as the deformed one and a Δl of -3 lbs is used to set the reference hologram. As an example, if the displacement map for 100 lbs of load is required, the holograms at 97 and 100 lbs will work as the reference and deformed holograms respectively. This helps to have the same Δl for all the displacement maps allowing comparisons among the four bone groups.

A comparison of the displacement maps at 100, 200 and 300 lbs is presented for each one of the analyzed groups (groups mentioned in section 4.3.2). Figure IV.7 shows the comparison between *m+ H2O* and *dm@4hrs + H2O* for each one of the selected compression values.

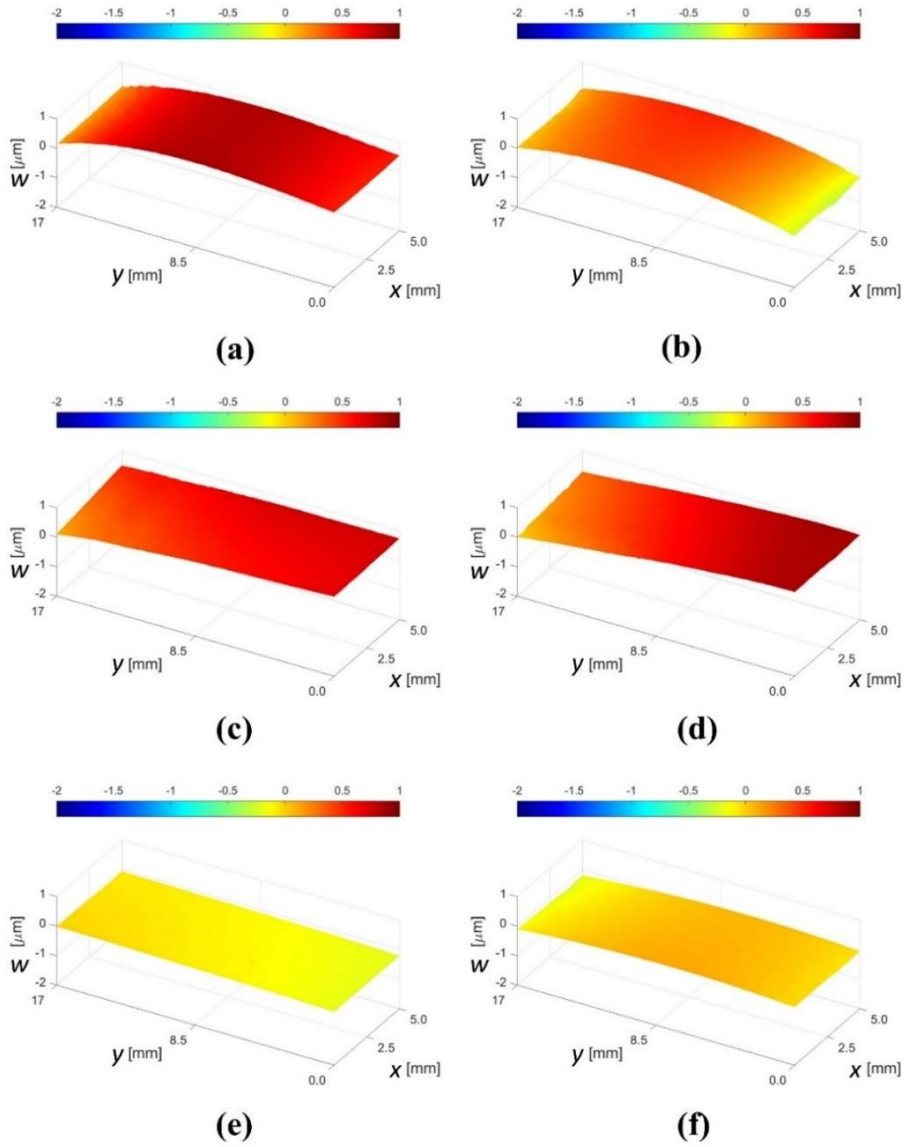

Fig. IV.7. Average surface displacement map comparison between m + H2O and dm@4hrs + H2O left and right column respectively, for (a,b) 100 (c,d) 200 and (e,f) 300 lbs.

From Fig. IV.7 it is possible to notice that well hydrated and mineralized bone samples (*m + H2O*) have a decreasing magnitude in displacement as the compression load increases. This surface response is replicated in the hydrated bone samples with a demineralization process of 4 hours. However, as these samples lost some of their hydroxyapatite, the water protects the natural anisotropy of the bone by keeping the internal collagen hydrated. The latter is observed with larger displacement

ranges and a smaller time required to reach the selected loads (see Table IV.3) if it is compared with the control group (i.e., Fig. IV.7 (a) compared with IV.7 (b)). Figure 8 shows the surface displacement comparison of the two dehydrated groups: *m-H2O@48hrs* and *dm@4hrs-H2O@48hrs.*

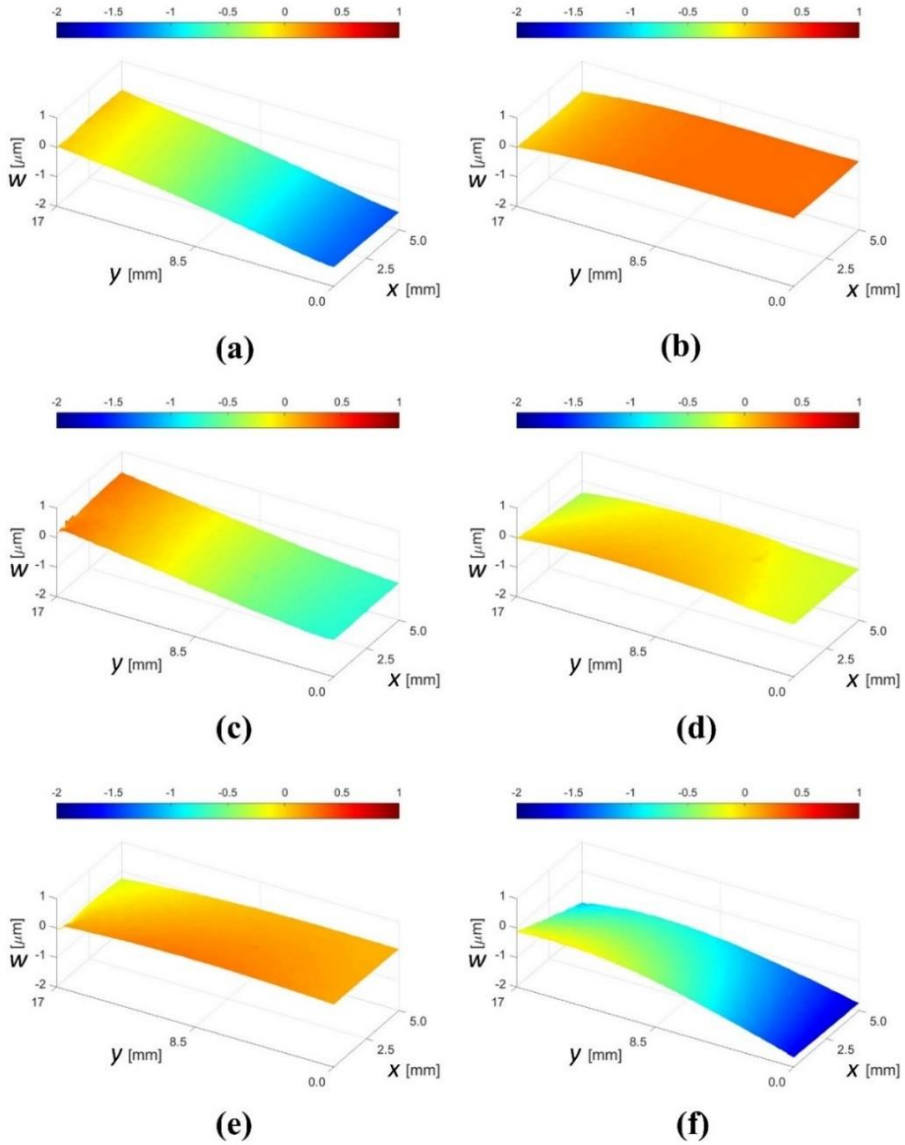

Fig. IV.8. Average surface displacement map comparison between m-H2O@48hrs and dm@4hrs-H2O@48hrs left and right column respectively, for (a,b) 100 (c,d) 200 and (e,f) 300 lbs.

The dehydrated groups show higher displacement magnitudes than those observed in Fig. IV.7. In the case of the average response of the *m-H2O@48hrs* group, the displacement at 100 lbs is larger than the one at 300 lbs. This displacement reduction looks similar to that of the control group, but in this case the magnitudes are approximately 5 times larger in every case. The average response of the *dm@4hrs-H2O@48hrs* group, which is affected in mineral, water and collagen, shows displacement magnitudes opposite to the control group. For this group as the compression load increases the surface displacement also increases. This indicates that bone's ability to deal with the compression load is no longer available. This can also be observed in terms of the time that each of these two groups consumes to reach the compressive load values. The demineralized groups are affected by the compression faster than the mineralized samples as Table IV.3 times indicate. The collagen is the main element in the *dm@4hrs-H2O@48hrs* group and gives not enough support to the bone's structure.

V. SUMMARY AND CONCLUSIONS

DHI conforms the most powerful technique among those based on speckle because it does not require any moveable element within its hardware besides that only two exposures are needed to calculate full-field displacements over the sample, fact that makes it ideal in fast mechanical evaluations, especially when the behavior of the sample is not repeatable such as in composite materials where non-linear and anisotropic natures do not permit to obtain similar mechanical responses under the same kind of mechanical excitation.

In this work, a wide study on cortical bone structure is presented based on surface displacement analysis under different conditions. The study is divided in two sections. The first section focuses on the characterization of cortical bone surface structure displacements when medical

drilling is practiced on the samples and a loss of bone volume is provoked. The possibility to observe these surface displacements in porcine bones (femur) at physiological and overload compression loads using a high-speed DHI system was demonstrated. A surface displacement comparison for healthy non-drilled and drilled bones is presented. The comparison among the compression interest values was possible by setting an incremental overload of 5 lbs in all the cases as it is shown in fig. III.4. In this analysis the non-drilled bone tests are taken as the reference condition for comparison, as they exhibited good mechanical stability. Owing to the viscoelastic composition of the bone, it was necessary to analyze the deformation profiles for physiologic (up to 55 lbs of compression load) and overload (up to 405 lbs of compression load) regions separately. A clear difference between the physiological and overload results was manifested on the tests. For the first case, complex and high-magnitude patterns are observed, while in overloads, a trend to deform less as load increased is shown. When overload is reached the complete surface of the bone is saturated with compression loads and there is no more structural area to re-arrange by itself in order to free loading forces. Even when non-drilled bones exhibit a trend on the direction they deform, the anisotropic nature is present for physiologic ranges and to a lesser extent for overload ranges. This anisotropic nature of the bone is pronounced when bone samples are drilled. Under this condition for physiologic load regions, the trend to deform in a consistent direction such as it occurs in non-drilled samples is no longer present; the magnitudes of deformation patterns are increased showing a weakening of the cortical bone structure and revealing a relationship between compression load and bone volume loss due to the drilling. This can be assumed as “lower compression values and fewer drillings create higher surface displacements, while higher compression values and more drillings result in smaller surface displacements.” It is important not to confuse this behavior with a hardening of the bone structure. The bone’s volume loss increases the stiffness of the bone and decreases its rearrangement capability for creating small displacements with higher-strain concentrations. This creates a more fragile structure, which cannot modify itself during a compression, and microfractures start to take place as

it is shown in Fig. III.12 where the direction in which the micro-fractured structure deforms should have a direct influence in the medical screw holding, giving rise to common screw-loosening phenomena and making DHI a viable technique to study the conditions that avoid the screw from loosening during medical procedures of this kind.

In the second section, encouraged by these previous results, an analysis of the strength secondary affectations (beyond osteoporosis) is made in bovine cortical bone and presented in terms of compression load tests. Several samples were machined for each one of four groups that emulate the secondary affectations of bone strength. More than twenty conditions and diseases may affect the bone's strength in *quantity*, *quality* and *turnover*, thus, two different protocols were investigated and designed to degrade, independently, one or more of the bone's principal components (organic or inorganic). Demineralization and air-dried protocols were applied to modify the hydroxyapatite and the collagen-water contents, and they were tested by means of the FT-IR transmittance spectral signal which is shown in Figs. IV.3 and IV.4 respectively. An out of plane DHI system was used to record image holograms in order to retrieve the optical amplitude and phase that is transformed into the surface displacement map. This displacement information is used for comparison purposes among the four bone groups, and indeed to corroborate the mechanical behavior of the bones. The compression test was performed by means of a Micro Compressive Testing Machine (MCTM) specifically designed for optical non-destructive testing which simplified the matching with the high-speed camera recordings. The MCTM applied linear temporal compression steps by using an embedded control, what permitted to differentiate the non-linear response from the bone samples respect to the mechanical deformation signal. A compression load range between 30 and 300 lbs was selected to start in the physiological range up to an overload of 40 times for the selected cattle. Two types of analysis are shown for the bone samples: temporal response (Fig. IV.5) and surface displacement (Figs. IV.7 and IV.8). In the temporal loading tests two zones are identified with respect

to the control group if the mineral component is considered as reference. These regions imply the required time for a bone sample to reach certain compression value, being the dehydrated-demineralized bones those that reach it faster. The mineralized and air-dried bones showed more opposition to be compressed because their stiffness is increased but became more susceptible to a sudden break without permanent deformations before (especially observable in Fig. IV.8(c)). In this case they behave like a crystal and the strength is strongly compromised with respect to the control group. The demineralized bones with compromised organic phases reduced their support capabilities; in this case the structure becomes more malleable. This is evident by observing the surface displacement which shows the dominion of the elastic properties in medium and high loads (Figs. IV.8(d) and IV.8(f) respectively).

An average surface displacement of several samples per group was computed and shown in Figs. IV.7 and IV.8. The mechanical response of the composite structure was better understood based on this full-field displacement information. The affectation protocols help to separate the mechanical influence of a missing component in the bone samples. The results obtained proved the theory for a strong integration existence among the hydroxyapatite, collagen and water, which determines the bone strength (more than just bone quantity as in the case of osteoporosis). Then, the way in that strength is modified by removing any of these bone components is shown by the surface variation that the sample suffers during a compression. This work also showed that DHI is a functional technique to analyze strength in mechanical ex-vivo biomaterials (bio and composite materials) where the presence or lack of each one of the essential elements determines the material mechanical response. Finally, in the results of this work it was observed that hydration is also a relevant factor that modifies the bone's mechanical structure to support compression loads, giving a possible answer for the question 'why ancient people with normal mineral content in their bones still experience fractures?

REFERENCES

[1] Thompson DW. “On growth and form”. 2nd ed., reprinted. Cambridge: Cambridge University Press; 1968.

[2] Currey JD. “Bones: structure and mechanics”. New Jersey: Princeton University Press; 2002.

[3] Vincent JFV. “Structural biomaterials”. revised ed. New Jersey: Princeton University Press; 1991.

[4] Srinivasan AV, Haritos G. Hedberg Appl Mech Rev 1991;44:463–82.

[5] Sarikaya M. Micro Res Tech 1994;27:360–75.

[6] Marc A. Meyers *, Po-Yu Chen. Biological materials: Structure and mechanical properties. Progress in Materials Science 53 (2008) 1–206.

[7] K. Grandfield, “Bone, implants and their interfaces,” Phys. Today 68(4), 40–45 (2015).

[8] S. Li, E. Demirci, and V. V. Silberschmidt, “Variability and anisotropy of mechanical behavior of cortical bone in tension and compression,” J. Mech. Behav. Biomed. Mater. 21, 109–120 (2013).

[9] D. T. Reilly and A. H. Burstein, “The elastic and ultimate properties of compact bone tissue,” J. Biomech. 8, 393–405 (1975).

[10] P. Zioupos, J. D. Currey, M. S. Mirza, and D. C. Barton, “Experimentally determined microcracking around a circular hole in a flat-plate of bone: comparison with predicted stresses,” Philos. Trans. R. Soc. London B Biol. Sci. 347, 383–396 (1995).

[11] Shull Peter, Nondestructive Evaluation Theory, Techniques, and Applications, 1st ed. Pennsylvania, 2001.

[12] Y. K. Zhu, G. Y. Tian, R. S. Lu, and H. Zhang, “A review of optical NDT technologies,” Sensors, vol. 11, no. 8, pp. 7773–7798, 2011.

[13] I. M. De la Torre, M. del S. Hernández Montes, J. M. Flores-Moreno, and F. M. Santoyo, “Laser speckle based digital optical methods in structural mechanics: A review,” Opt. Lasers Eng., vol. 87, pp. 32–58, 2015.

[14] K. J. Gasvik, Optical metrology. 2002.

[15] G. Cloud, Optical methods of engineering analysis, First edit. Cambridge University Press, 1995.

[16] W. A. James F. Shackelford, Materials science and engineering handbook, Third edit. CRC Press, 2001.

[17] Roy R. Graig. Jr., Mechanics of materials, First edit. John Wiley & Sons, Inc, 1996.

[18] K. Ralls, Introduction to materials science and engineering, First edit. Taipei, 1977.

[19] J. Sanchez-Horneros, "La industria aeronáutica y los materiales compuestos," Hispaviación, 2015.

[20] J. C. A. Islas, "Estudio de aleación de aluminio reforzada con materiales compuestos para reducción de peso en la industria automotriz," 2013.

[21] M. Grédiac, "The use of full-field measurement methods in composite material characterization: Interest and limitations," Compos. Part A Appl. Sci. Manuf., vol. 35, no. 7–8, pp. 751–761, 2004.

[22] M. Bonnet, H. D. Bui, and A. Constantinescu, "Principes variationnels et exploitation de measure de champs en élasticite," Mec. Ind., vol. 4, no. 6, pp. 687–697, 2003.

[23] B. M. R. Young, B. Tolbert, and M. F. Utter, "Bulletin de la S.M.F.," vol. 60, no. 1964, pp. 250–258, 1966.

[24] R. F. MacBarb, A. L. Chen, J. C. Hu, and K. A. Athanasiou, "Engineering functional anisotropy in fibrocartilage neotissues," Biomaterials, vol. 34, no. 38, pp. 9980–9989, Dec. 2013.

[25] T. M. and M. F. Y. Morimoto, "Application of three-dimensional displacement and strain distribution measurement by windowed phase-shifting digital holographic interferometry," Adv. Mater. Res., vol. 47–50, pp. 1262–1265, 2008.

[26] G. R. and P. R. Sai Siva Gorthi, "Strain estimation in digital holographic interferometry using piecewise polynomial phase approximation based method," Opt. Express, vol. 18, no. 2, pp. 560–565, 2010.

[27] F. Mendoza S. M. De la Torre-Ibarra, "Surface strain distribution on thin metallic plates using 3-D digital holographic interferometry," Opt. Eng., vol. 45, no. 10, p. 105603, 2006.

[28] J. D. Currey, "Biomechanics of Mineralized Skeletons," in Skeletal Biomineralization: Patterns, Processes and Evolutionary Trends, American Geophysical Union (AGU), 2013, pp. 11–25.

[29] T. A. Muller R., "Bone density and composition: age related and pathological changes in water and mineral content," J. Bone Jt. Surg., vol. 48, pp. 140–148, 1966.

[30] N. K. Lee, H. Sowa, E. Hinoi, M. Ferron, J. D. Ahn, R. Dacquin, P. J. Mee, M. D. Mckee, D. Y. Jung, J. K. Kim, F. Mauvais-jarvis, P. Ducy, and G. Karsenty, "<Lee-2007-Endocrine regulation.pdf>," vol. 130, no. 3, pp. 456–469, 2007.

[31] J.-Y. Rho, L. Kuhn-Spearing, and P. Zioupos, "Mechanical properties and the hierarchical structure of bone," Med. Eng. Phys., vol. 20, no. 2, pp. 92–102, 1998.

[32] D. Felsenberg and S. Boonen, "The bone quality framework: Determinants of bone strength and their interrelationships, and implications for osteoporosis management," Clin. Ther., vol. 27, no. 1, pp. 1–11, 2005.

[33] Paolo Vannucci, "Anisotropic Elasticity". Springer. Singapore 2018.

[34] Z. Fan a, J.G. Swadener . Anisotropic properties of human tibial cortical bone as measured by nanoindentation. Journal of Orthopaedic Research 20 (2002).

[35] J. W. Goodman, Introduction to Fourier optics, 2nd ed. New York, NY, USA: McGraw-Hill, 1996.

[36] Max Born and Emil Wolf, Principles of Optics, 7th ed. Cambridge University Press, 1999.

[37] R. Jones and C. Wykes, Holographic and Speckle Interferometry. publisherNameCambridge University Press, 1989.

[38] U. Schnars and W. Jueptner, Digital Holography. Berlin, Heidelberg: SPRINGER, 2005.

[39] T. Kreis, Handbook of holographic Interferometry. Germany: Wiley, 2005.

[40] C. M. Vest, Holographic Interferometry, 1st ed. California: Wiley-Interscience, 1979.

[41] M. Takeda, H. Ina, and S. Kobayashi, "Fourier-transform method of fringe-pattern analysis for computer-based topography and interferometry," J. Opt. Soc. Am., vol. 72, no. 1, p. 156, 1982.

[42] H. J. T. Schedin S. , Pedrini G., "Simultaneous three-dimensional dynamic deformation measurements with pulsed digital holography," Appl. Opt., vol. 38, no. 34, 1999.

[43] F. M. Santoyo, G. Pedrini, S. Schedin, and H. J. Tiziani, "3D displacement measurements of vibrating objects with multi-pulse digital holography," Meas. Sci. Technol., vol. 10, no. 12, pp. 1305–1308, Dec. 1999.

[44] G. Murali Krishna, et al. “A critical review on fundamental and pharmaceutical analysis of ft-ir spectroscopy” Int J. Pharm 3(2): 396-402. 2013;

[45] R. K. Pandey and S. S. Panda, “Drilling of bone: A comprehensive review,” J. Clin. Orthop. Trauma, vol. 4, no. 1, pp. 15–30, 2013.

[46] S. Karmani, “The thermal properties of bone and the effects of surgical intervention,” Current Orthopaedics, vol. 20, no. 1. pp. 52–58, 2006.

[47] H. W. Maurice E. Müller, Martin Allgöwer, Robert Schneider, Manual of Internal Fixation, 3rd ed. Berlin, Heidelberg, New York: SPRINGER, 1991.

[48] Marti, C. Fankhauser, A Frenk, J. Cordey, and B. Gasser, “Biomechanical evaluation of the less invasive stabilization system for the internal fixation of distal femur fractures,” J. Orthop. Trauma, vol. 15, no. 7, pp. 482–487, 2001.

[49] R. L. Uhl, “The biomechanics of screws.,” Orthop. Rev., vol. 18, pp. 1302–1307, 1989.

[50] T. De Marco, M. Peccarisi, F. Conversano, A. Greco, S. Chiozzi, F. De Pascalis, and S. Casciaro, “A new approach for measuring the trabecular bone density through the echosound backscattering: An ex vivo validation on human femoral heads,” Measurement, vol. 87, pp. 51–61, 2016.

[51] L. V. Coutts, T. Jenkins, T. Li, D. G. Dunlop, R. O. C. Oreffo, C. Cooper, N. C. Harvey, P. J. Thurner, N. K. Arden, J. M. Latham, P. Taylor, M. Baxter, N. Moss, C. Ball, and K. Chan, “Variability in reference point microindentation and recommendations for testing cortical bone: Location, thickness and orientation heterogeneity,” J. Mech. Behav. Biomed. Mater., vol. 46, pp. 292–304, 2015.

[52] J. J. Schwiedrzik and P. K. Zysset, “Quantitative analysis of imprint shape and its relation to mechanical properties measured by microindentation in bone,” J. Biomech., vol. 48, no. 2, pp. 210–216, 2015.

[53] J. J. Elsner, M. Shemesh, A. Shefy-Peleg, Y. Gabet, E. Zylberberg, and E. Linder-Ganz, "Quantification of in vitro wear of a synthetic meniscus implant using gravimetric and micro-CT measurements," J. Mech. Behav. Biomed. Mater., vol. 49, pp. 310–320, 2015.

[54] S.-H. Kim, J.-W. Shin, S.-A. Park, Y. K. Kim, M. S. Park, J. M. Mok, W. I. Yang, and J. W. Lee, "Chemical, structural properties, and osteoconductive effectiveness of bone block derived from porcine cancellous bone.," J. Biomed. Mater. Res. Part B Appl. Biomater., vol. 68, no. 1, pp. 69–74, 2004.

[55] A. Dalla Pria Bankoff, "Biomechanical Characteristics of the Bone," Hum. Musculoskelet. Biomech., pp. 61–86, 2012.

[56] S. F. Hodgson et. al., "American Association of Clinical Endocrinologists medical guidelines for clinical practice for the prevention and treatment of postmenopausal osteoporosis: 2001 edition, with selected updates for 2003," Endocr. Pr., vol. 9, no. 6, pp. 544–564, 2001.

[57] M. R. Hardisty, M. A. Soicher, T. C. Garcia, S. M. Stover, and D. P. Fyhrie, "Do stress-whitening and optical clearing of collagenous tissue occur by the same mechanism?," J. Biomech., vol. 46, no. 14, pp. 2411–2418, 2013.

[58] M. L. Bouxsein, "Determinants of skeletal fragility," Best Pract. Res. Clin. Rheumatol., vol. 19, no. 6, pp. 897–911, 2005.

[59] A. Maghraoui, "Interpreting a DXA Scan in Clinical Practice, Dual Energy X-ray Absorptiometry," Dual Energy X-Ray Absorptiometry, no. Roux 1998, p. 146, 2012.

[60] N. B. Watts, "Fundamentals and pitfalls of bone densitometry using dual-energy X-ray absorptiometry (DXA)," Osteoporos. Int., vol. 15, no. 11, pp. 847–854, 2004.

[61] S. R. Cummings, D. B. Karpf, F. Harris, H. K. Genant, K. Ensrud, A. Z. LaCroix, and D. M. Black, "Improvement in spine bone density and reduction in risk of vertebral fractures during treatment with antiresorptive drugs," Am. J. Med., vol. 112, no. 4, pp. 281–289, Feb. 2002.

[62] T. E. Dufresne, P. A. Chmielewski, M. D. Manhart, T. D. Johnson, and B. Borah, “Risedronate Preserves Bone Architecture in Early Postmenopausal Women In 1 Year as Measured by Three-Dimensional Microcomputed Tomography,” Calcif. Tissue Int., vol. 73, no. 5, pp. 423–432, Oct. 2003.

[63] E. M. Lochmüller, J. B. Zeller, D. Kaiser, F. Eckstein, J. Landgraf, R. Putz, and R. Steldinger, “Correlation of femoral and lumbar DXA and calcaneal ultrasound, measured in situ with intact soft tissues, with the in vitro failure loads of the proximal femur,” Osteoporos. Int., vol. 8, no. 6, pp. 591–598, 1998.

[64] S. C. E. Schuit, M. Van Der Klift, A. E. A. M. Weel, C. E. D. H. De Laet, H. Burger, E. Seeman, A. Hofman, A. G. Uitterlinden, J. P. T. M. Van Leeuwen, and H. A. P. Pols, “Fracture incidence and association with bone mineral density in elderly men and women: The Rotterdam Study,” Bone, vol. 34, no. 1, pp. 195–202, 2004.

[65] S. ES, Y. Chen, A. TA, and et al, “Bone mineral density thresholds for pharmacological intervention to prevent fractures,” Arch. Intern. Med., vol. 164, no. 10, pp. 1108–1112, May 2004.

[66] E. Sornay-Rendu, F. Munoz, P. Garnero, F. Duboeuf, and P. D. Delmas, “Identification of osteopenic women at high risk of fracture: The OFELY study,” J. Bone Miner. Res., vol. 20, no. 10, pp. 1813–1819, 2005.

[67] A. Unnanuntana, B. J. Rebolledo, M. Michael Khair, E. F. Dicarlo, and J. M. Lane, “Diseases affecting bone quality: Beyond osteoporosis,” Clin. Orthop. Relat. Res., vol. 469, no. 8, pp. 2194–2206, 2011.

[68] NIH Consensus Development Panel on, “Osteoporosis Prevention, Diagnosis, and Therapy,” JAMA, vol. 285, no. 6, pp. 785–795, 2001.

[69] S. M. H. Xia, P. Picart, “Mechanical behavior of CAD/CAM occlusal ceramic reconstruction assessed by digital color holography,” Dent. Mater., vol. 34, no. 8, pp. 1222–1234, 2018.

[70] H. Sugiyama, Y. T. Kim, Osteoporosis in Orthopedics: Assessment and Therapeutic Options, 1st ed., Japan, 2016.

[71] D. a Bushinsky, “Bone disease in moderate renal failure: cause, nature and prevention.,” Annu. Rev. Med., vol. 48, pp. 167–176, 1997.

[72] C. E. Fiore, P. Pennisi, F. Ciffo, C. Scebba, A. Amico, and S. Di Fazzio, “Immobilization-dependent bone collagen breakdown appears to increase with time: evidence for a lack of new bone equilibrium in response to reduced load during prolonged bed rest.,” Horm. Metab. Res., vol. 31, no. 1, pp. 31–36, Jan. 1999.

[73] Y. Zehnder, M. Luthi, D. Michel, H. Knecht, R. Perrelet, I. Neto, M. Kraenzlin, G. Zach, and K. Lippuner, “Long-term changes in bone metabolism, bone mineral density, quantitative ultrasound parameters, and fracture incidence after spinal cord injury: A cross-sectional observational study in 100 paraplegic men,” Osteoporos. Int., vol. 15, no. 3, pp. 180–189, 2004.

[74] E. Cleiren, O. Benichou, E. Van Hul, J. Gram, J. Bollerslev, F. R. Singer, K. Beaverson, A. Aledo, M. P. Whyte, T. Yoneyama, M. C. deVernejoul, and W. Van Hul, “Albers-Schonberg disease (autosomal dominant osteopetrosis, type II) results from mutations in the ClCN7 chloride channel gene.,” Hum. Mol. Genet., vol. 10, no. 25, pp. 2861–2867, Dec. 2001.

[75] S. G. Waguespack et. al., “Chloride channel 7 (ClCN7) gene mutations and autosomal dominant osteopetrosis, type II,” J. Bone Miner. Res., vol. 18, no. 8, pp. 1513–1518, 2003.

[76] W. J. Landis, K. J. Hodgens, M. J. Song, J. Arena, S. Kiyonaga, M. Marko, C. Owen, and B. F. McEwen, “Mineralization of collagen may occur on fibril surfaces: Evidence from conventional and high-voltage electron microscopy and three-dimensional imaging,” J. Struct. Biol., vol. 117, no. 1, pp. 24–35, 1996.

[77] A. H. Burstein, J. M. Zika, K. G. Heiple, and L. Klein, “Contribution of collagen and mineral to the elastic-plastic properties of bone.,” J. Bone Joint Surg. Am., vol. 57, no. 7, pp. 956–961, Oct. 1975.

[78] J. D. Currey, “The relationship between the stiffness and the mineral content of bone,” J. Biomech., vol. 2, no. 4, pp. 477–480, 1969.

[79] J. D. Currey, “Strain rate and mineral content in fracture models of bone.,” J. Orthop. Res., vol. 6, no. 1, pp. 32–38, 1988.

[80] S. Calve, I. F. Lytle, K. Grosh, D. L. Brown, and E. M. Arruda, “Implantation increases tensile strength and collagen content of self-assembled tendon constructs.,” J. Appl. Physiol., vol. 108, no. 4, pp. 875–881, 2010.

[81] R. M. Natoli, S. Skaalure, S. Bijlani, K. X. Chen, J. Hu, and K. A. Athanasiou, “Intracellular Na+ and Ca2+ modulation increases the tensile properties of developing engineered articular cartilage,” Arthritis Rheum., vol. 62, no. 4, pp. 1097–1107, 2010.

[82] C. H. Turner, “Bone strength: Current concepts,” Ann. N. Y. Acad. Sci., vol. 1068, no. 1, pp. 429–446, 2006.

[83] O. Di Munno, A. Delle Sedie, M. Rossini, and S. Adami, “Disease-modifying antirheumatic drugs and bone mass in rheumatoid arthritis.,” Clin. Exp. Rheumatol., vol. 23, no. 2, pp. 137–144, 2005.

[84] H.-J. Kim, H. Zhao, H. Kitaura, S. Bhattacharyya, J. A. Brewer, L. J. Muglia, F. P. Ross, and S. L. Teitelbaum, “Glucocorticoids suppress bone formation via the osteoclast,” J. Clin. Invest., vol. 116, no. 8, pp. 2152–2160, Aug. 2006.

[85] J. J. Stepan, D. B. Burr, I. Pavo, A. Sipos, D. Michalska, J. Li, A. Fahrleitner-Pammer, H. Petto, M. Westmore, D. Michalsky, M. Sato, and H. Dobnig, “Low bone mineral density is associated with bone microdamage accumulation in postmenopausal women with osteoporosis,” Bone, vol. 41, no. 3, pp. 378–385, 2007.

[86] M.-Y. Weng and N. E. Lane, “Medication-induced osteoporosis.,” Curr. Osteoporos. Rep., vol. 5, no. 4, pp. 139–145, Dec. 2007.

[87] H. Birkedal-Hansen, “Diffusion of H36Cl in decalcified ivory dentine,” J. Histochem. Cytochem., vol. 022, p. 428, 1974.

[88] H. Birkedal Hansen, “Kinetics of acid demineralization in histologic technique,” J. Histochem. Cytochem., vol. 22, no. 6, pp. 434–441, 1974.

[89] A. B. Castro-Ceseña, E. E. Novitskaya, P. Y. Chen, G. A. Hirata, and J. McKittrick, “Kinetic studies of bone demineralization at different HCl concentrations and temperatures,” Mater. Sci. Eng. C, vol. 31, no. 3, pp. 523–530, 2011.

[90] M. Granke, M. D. Does, and J. S. Nyman, “The Role of Water Compartments in the Material Properties of Cortical Bone,” Calcif. Tissue Int., vol. 97, no. 3, pp. 292–307, 2015.

[91] A. Faingold, S. R. Cohen, R. Shahar, S. Weiner, L. Rapoport, and H. D. Wagner, “The effect of hydration on mechanical anisotropy, topography and fibril organization of the osteonal lamellae,” J. Biomech., vol. 47, no. 2, pp. 367–372, 2014.

[92] F. G. Evans and M. Lebow, “Regional Differences in Some of the Physical Properties of the Human Femur,” J. Appl. Physiol., vol. 3, no. 9, pp. 563–572, 1951.

[93] J. J. Broz, S. J. Simske, A. R. Greenberg, and M. W. Luttges, “Effects of Rehydration State on the Flexural Properties of Whole Mouse Long Bones,” J. Biomech. Eng., vol. 115, no. 4A, pp. 447–449, Nov. 1993.

[94] P. Y. Chen, D. Toroian, P. A. Price, and J. McKittrick, “Minerals form a continuum phase in mature cancellous bone,” Calcif. Tissue Int., vol. 88, no. 5, pp. 351–361, 2011.

[95] P. Y. Chen and J. McKittrick, “Compressive mechanical properties of demineralized and deproteinized cancellous bone,” J. Mech. Behav. Biomed. Mater., vol. 4, no. 7, pp. 961–973, 2011.

[96] G. E. Fantner, H. Birkedal, J. H. Kindt, T. Hassenkam, J. C. Weaver, J. A. Cutroni, B. L. Bosma, L. Bawazer, M. M. Finch, G. A. G. Cidade, D. E. Morse, G. D. Stucky, and P. K. Hansma, “Influence of the degradation of the organic matrix on the microscopic fracture behavior of trabecular bone,” Bone, vol. 35, no. 5, pp. 1013–1022, 2004.

[97] D. Toroian, E. L. Joo, and P. A. Price, “The size exclusion characteristics of type I collagen: Implications for the role of noncollagenous bone constituents in mineralization,” J. Biol. Chem., vol. 282, no. 31, pp. 22437–22447, 2007.

[98] R. Lakes, “Materials with structural hierarchy,” Nature, vol. 361, p. 511, Feb. 1993.

[99] S. Weiner and H. D. Wagner, “THE MATERIAL BONE: Structure-Mechanical Function Relations,” Annu. Rev. Mater. Sci., vol. 28, no. 1, pp. 271–298, 1998.

[100] P. Y. Chen, A. Y. M. Lin, Y. S. Lin, Y. Seki, A. G. Stokes, J. Peyras, E. A. Olevsky, M. A. Meyers, and J. McKittrick, “Structure and mechanical properties of selected biological materials,” J. Mech. Behav. Biomed. Mater., vol. 1, no. 3, pp. 208–226, 2008.

[101] K. U. Lewandrowski, V. Venugopalan, W. W. Tomford, K. T. Schomacker, H. J. Mankin, and T. F. Deutsch, “Kinetics of cortical bone demineralization: controlled demineralization--a new method for modifying cortical bone allografts.,” J. Biomed. Mater. Res., vol. 31, no. 3, pp. 365–372, Jul. 1996.

[102] C. R. Galia, A. L. Lourenço, R. Rosito, C. A. Souza Macedo, and L. M. A. Q. Camargo, “Physicochemical Characterization of Lyophilized Bovine Bone Grafts,” Rev. Bras. Ortop. (English Ed., vol. 46, no. 4, pp. 444–451, 2011.

[103] J. A. F. G. M.M. Figueiredo and A. G. Martins, “Characterization of Bone and Bone-Based

Graft Materials Using FTIR Spectroscopy," in Infrared Spectroscopy - Life and Biomedical Sciences, P. T. T. (Ed.), Ed. 2012, pp. 315–334.

[104] A. Dalla Pria Bankoff, "Biomechanical Characteristics of the Bone," Hum. Musculoskelet. Biomech., pp. 61–86, 2012.

[105] A. D. P. Bankoff, Morfologia e cinesiologia aplicada ao movimento humano. Rio de Janeiro, 2007.

APPENDIX

Bone sample preparation

As it is mentioned before, we study cortical bone in that it represents a complex Biological Material where structures with different dimensions at organic and inorganic phases make it an interesting matter of study under different conditions. At the first part of the work (exposed in Chapter III) we analyze how the cortical drilling process affects the surface's structural response of a large bone. A study in porcine femoral bones with and without the presence of cortical drillings is performed. The analyzed bones correspond to porcine strain *Landrace*. They are less than 24 hour post-mortem samples from healthy non-drilled femurs from the back leg of male animals with a weight rank between 195 and 205 lbs and about five months old. The first step of the bone preparation begins at the butcher shop. The fresh femur is partially cleaned from muscles and other tissues and then, cutted with a hand knife to separate their extremes which contain the spongy bone (see Fig. III.1). The resulted diaphyses, which are around 90 mm of length, are submerged in soft chlorine water solution (1%) for about 120 min. This helps to finely clean out the thin muscle and connective tissues using a scalpel to get a whiter bone surface and at the same time, to avoid damage on it such as in the case of concentrated acid solutions. As the experiment requires that the bone extremes adequately match the flat supports that connect a load cell and the moving part of a mechanical press to transmit the compression axially through the bone (see Fig. III.3), a low speed grind-mill drilling machine is used to grind the diaphysis extremes. Some of its outstanding features are listed below and the corresponding machine is depicted in Fig. A1.

- Cammac ZX45 Mill Drill
- 6 Speed 6-1250 rpm
- Worktable size: 800mm x 240mm
- 45mm Drilling Capacity
- 90° Head Tilt Left & Right
- Coolant & Worklamp

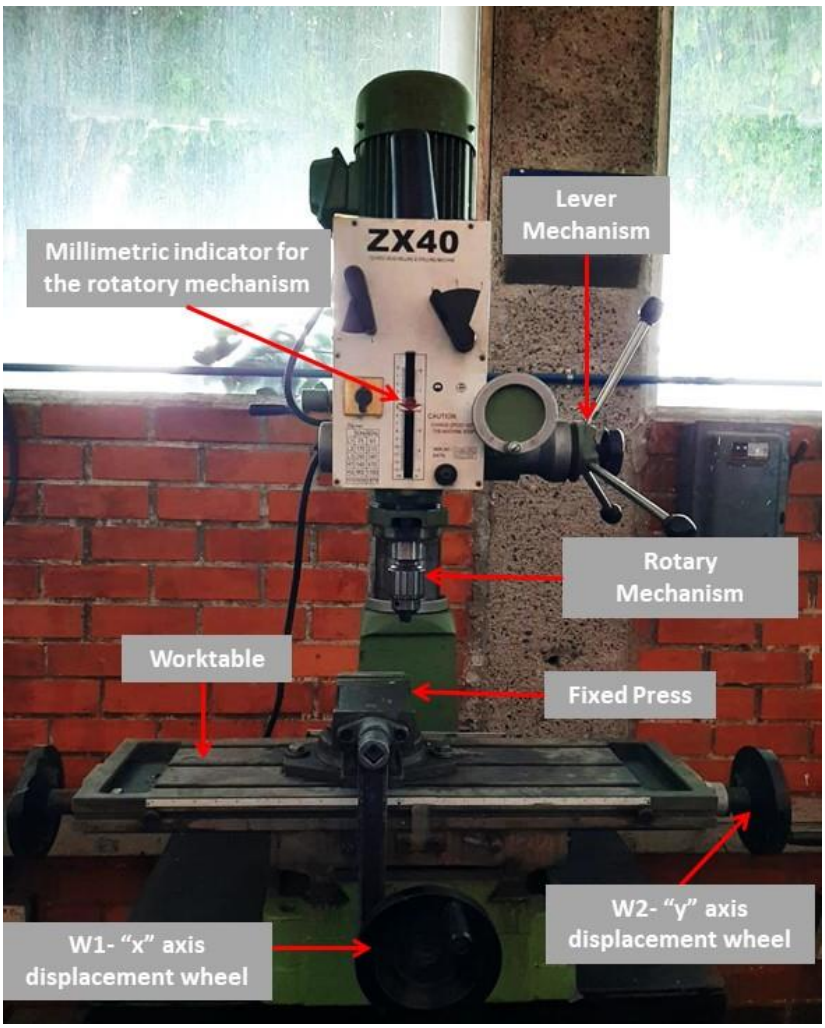

Fig.A.1. Grind mill drilling machine employed to shape the final bone samples for the experiments.

The first of the grinding bone steps consists on grip the bone sample vertically over the fixed press at the worktable's machine by mean of a couple of curved plates that fix the bone in the xy plane as it is shown in Fig. A2

Afterwards, a diamond drill bit is coupled to the machine's rotatory mechanism and the lower velocity is selected (6 rpm) to minimize the heat generation. The machine is then turned on. The drill bit approaches in millimetric steps to the bone by means of a lever mechanism especially designed for it. When the tip of the drill contacts the bone surface, a controlled displacement over the xy plane is applied to the worktable by using the wheels w1 and w2 (see Fig. A1) in order to grind the respective bone face along both directions completely. Once the face of the diaphysis has been grinded totally over the xy plane, the machine is stopped and the bone is turned axially in order to expose its non-grinded extreme to the rotary mechanism (along z axis in Fig. A2). As the horizontal plane of the fixed press now supports the first grinded extreme of the bone, it performs a reference plane that guarantee parallelism between final diaphysis' extremes for the test.

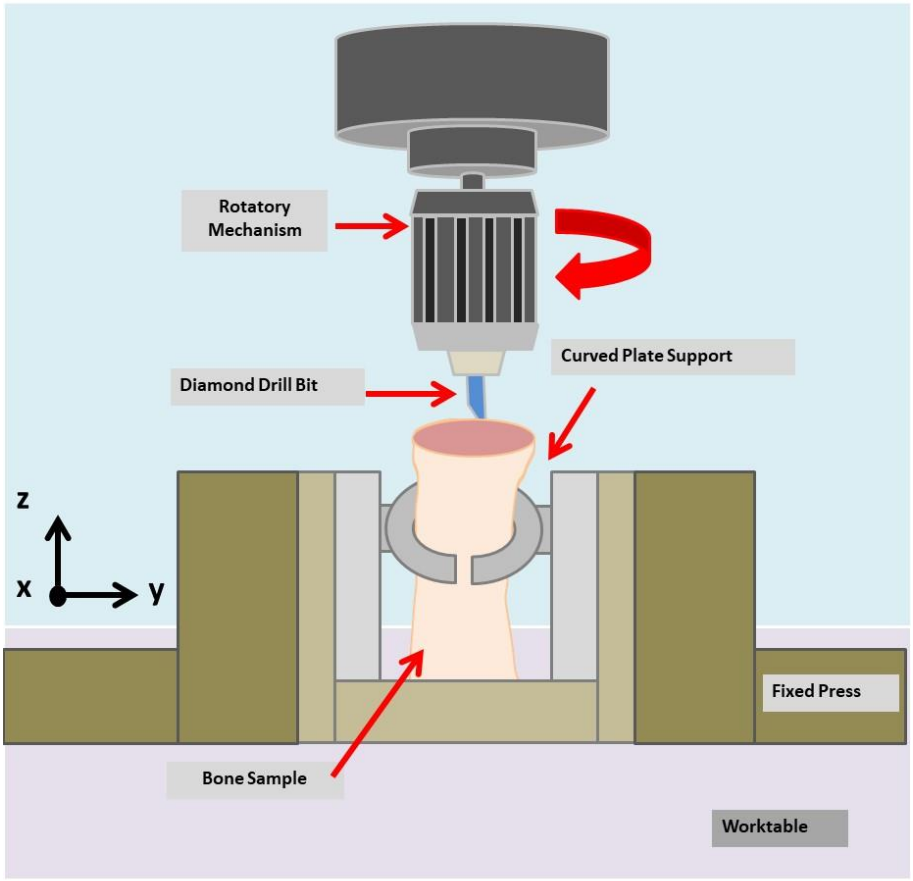

Fig. A2. Bone extreme face machined over the xy plane. The horizontal support of the first grinded extreme of the bone guarantees parallelism between final diaphysis' extremes for the test.

In the other hand, as some cortical samples must be drilled in order to compare them to the control group (non-drilled samples), the diaphyses are then placed over a wood platform and then fixed to it by means of a couple of plastic straps. The platform is placed over the machine´s worktable and then gripped against its fixed press as it is shown in Fig. A3. Drill bits with 4.5 mm and 6.5 mm of diameter are coupled (separately) to the rotatory mechanism of the machine and then the drillings are performed over the cortical bone by applying the lever mechanism (above mentioned) in a perpendicular manner to the bone's longitudinal direction. The lower velocity (6 rpm) is still

employed. The separation among perforations consists of 12 mm of length as the respective prosthetic devices requires.

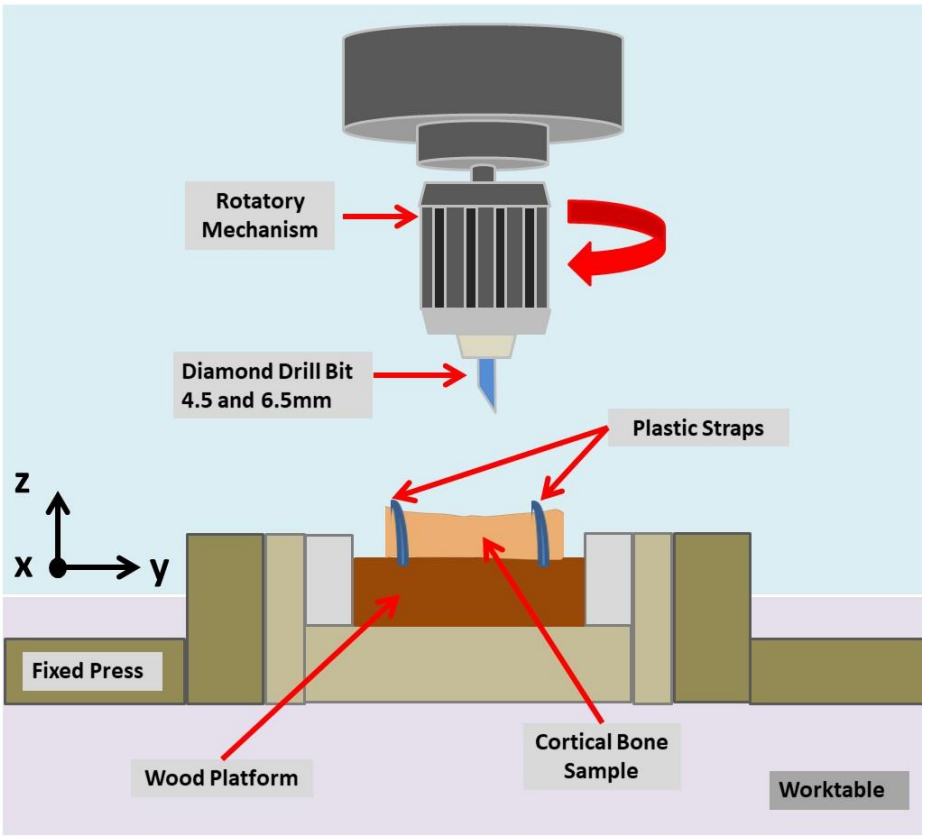

Fig. A3. Cortical Bone Drilling arrange for 4.5 and 6.5 mm of diameter

It is important to mention that before, during and after the entire machining process, the samples were kept fresh and wet using a 0.1 M phosphate-buffered saline solution (isotonic substance to preserve cellular tissues due to its osmolality). Even when the rotating diamond wheel machine was used, the bone samples were always irrigated with this solution.

At the second part of the work (exposure in Chapter IV), in order to study the bone strength, we analyze cortical bovine bone samples which are treated by means of demineralization and air-drying protocols to affect the mineral and organic phases respectively.

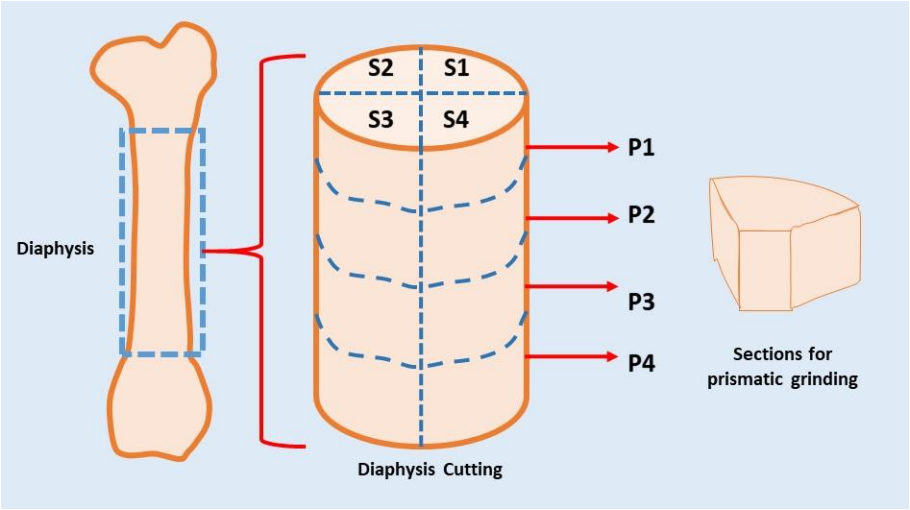

Fig. A4. Diaphysis Hand-Cutting. The Diaphysis is divided in four Parts ***[P1-4]****. Each Part is partitioned in four transversal sections* ***[S1-4],*** *in order to get 16 bone sections to be shaped into the final prismatic samples.*

The bovine femur bones were obtained locally at the butcher shop with less than 24 hrs post-mortem and all of them come from male bovine strain Angus, which are regular sized with an average weight of 1000 kg and bred for human consumption. The slaughter age of the cattle is approximately 20 months. These cortical bovine femur samples are obtained from the middle diaphysis by hand saw avoiding the use of electric devices which induce heat. The average mean transverse section of the diaphysis is 1960 mm^2. Each diaphysis is cutted in four parts (P) and then, each part is divided transversally in four *sections* (S) in order to prepare the final bone samples as it is shown in Fig. A4. All these femoral diaphysis *sections*, which length is around 20 mm, are submerged in spring water for about 90 minutes to easily clean out other thin tissues by using a scalpel. After that, the low speed grind-mill drilling machine, which is described above, is used to shape the samples. The cortical *sections* were carefully machined to a prismatic geometry of 5 × 5 × 17 mm. The first step of this procedure consists on directly grip the bone *sections* over the fixed press into a vertical direction (z-axis alignment) in order to fix the bone in the xy plane as it is shown in Fig. A5.

Afterwards, the diamond drill bit is coupled to the rotatory part of the machine and the lower velocity is selected (6 rpm) to minimize the heat generation. The drill bit is then approached to the superior extreme face of the bone section in millimetric steps by mean of the lever mechanism and when the tip of the drill bit contacts the bone surface, a controlled displacement over the xy plane is applied to the worktable in order to completely grind the respective bone face. When the superior face of the diaphysis has been grinded totally over the xy plane, the process is paused, and the bone is turned in order to expose its non-grinded extreme face to the rotatory drilling mechanism. As the horizontal plane of the fixed press now supports the first grinded extreme of the bone, it performs a reference plane that guarantees parallelism between final bone section extremes for the test.

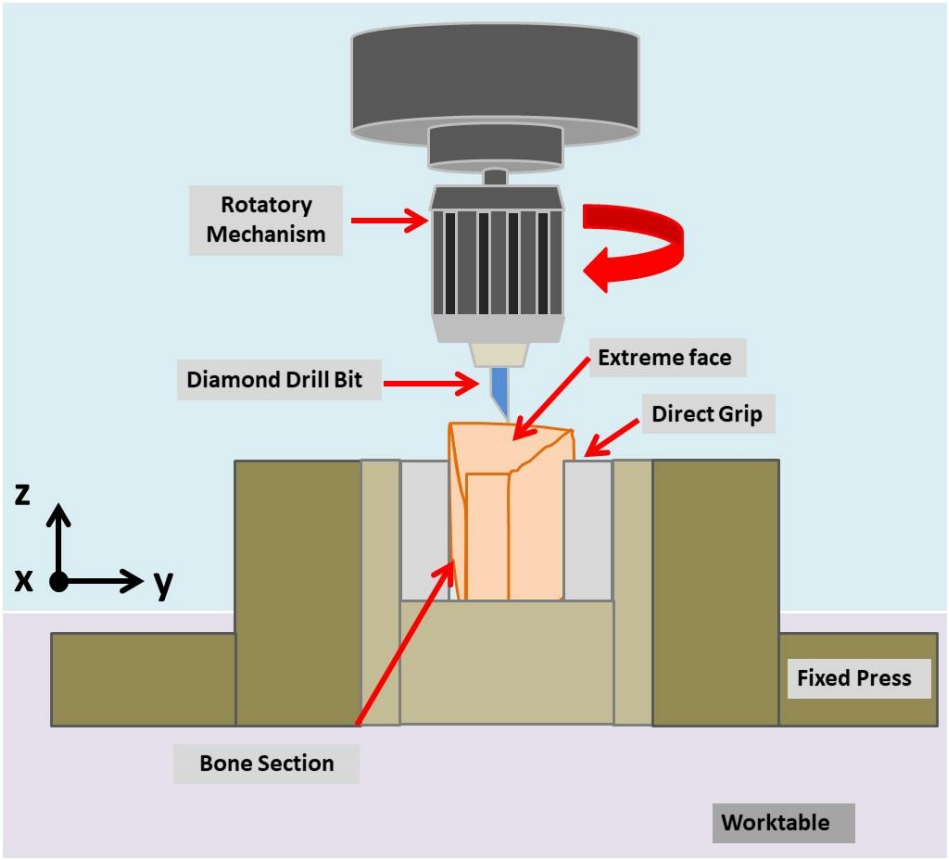

Fig. A5. Extreme faces grinding of the bone sections. The samples are aligned to z axis and directly gripped to the fixed press mechanism.

Once the two faces at the extremes of the sample have been grinded, the process is paused in order to directly grip the bone sample against the fixed press into a horizontal position (xy plane alignment) and then to grind the lateral sides of the bone section, see Fig. A6. The machine is turned on and the drill bit is then approached to the first of the four lateral sides of the bone sample in millimetric steps by mean of the lever mechanism of the rotating diamond wheel machine; when the tip of the drill contacts the bone, a controlled displacement over the xy plane is applied to the worktable in order to grind the respective bone side completely. Once the first lateral side of the sample has been grinded totally over the xy plane, the process is paused and the bone is turned horizontally over the xy plane in order to shape the second side of the bone sample by the rotatory drilling bit mechanism. The process is repeated until complete the prismatic geometry. The longest length of the samples (b = 17 mm) is selected to be aligned to the growth direction of the bone. The transverse section (a × a, 5 × 5 mm) of the final samples is selected considering the temporal model for the demineralization process described in Chapter IV.

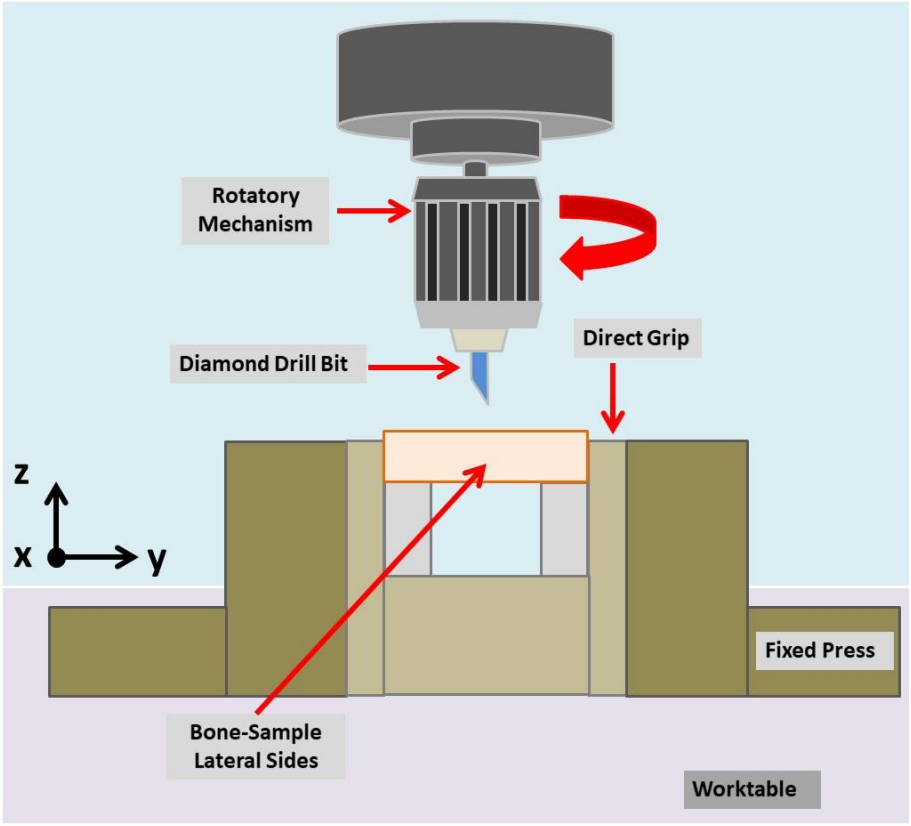

Fig. A6. Lateral sides shaping. The bone sections are aligned to xy plane (horizontally) and directly gripped to the fixed press mechanism.

It is important to point out that before, during and after the entire machining process, the samples were again kept fresh and wet using a 0.1 M phosphate-buffered saline solution (isotonic substance to preserve cellular tissues due to its osmolality). Even when the rotating diamond wheel machine was used, the bone samples were always irrigated with this solution.